ACCEPTED MANUSCRIPT

Title: Kinematics and strain distribution in an orogen-scale shear zone: insights from structural analyses and magnetic fabrics in the Gavarnie thrust, Pyrenees

Authors: Marcos Marcén [a,*], Antonio M. Casas-Sainz [a], Teresa Román-Berdiel [a], Belén Oliva-Urcia [b], Ruth Soto [c], Luca Aldega [d]

[a] Geotransfer, Dpto. Ciencias de la Tierra, Facultad de Ciencias, Instituto de Investigación en Ciencias Ambientales (IUCA), Universidad de Zaragoza, 50009 Zaragoza.

[b] Dpto. Geología y Geoquímica, Fac. Ciencias (6-406), Universidad Autónoma de Madrid, Ciudad Universitaria de Cantoblanco, 28049 Madrid, Spain.

[c] IGME, Instituto Geológico y Minero de España, Unidad de Zaragoza, 50006 Zaragoza.

[d] Dipartimento di Scienze della Terra, Sapienza Universita di Roma, 00185 Rome, Italy.

[*] Corresponding author: mma@unizar.es

Abstract

This work aims to characterize the Gavarnie thrust, one of the large-scale thrusts that define the Alpine structure of the west-central sector of the Pyrenees. A detailed comparison of structural analysis and magnetic fabrics is carried out for the Paleozoic phyllonites of the Gavarnie thrust, in order to decipher strain distribution and transport direction. The AMS at room (RT-AMS) and low (LT-AMS) temperature and the AIRM can be correlated with the structural patterns: k_{min} axes are mainly parallel to

the pole of the S, C or C' planes and k_{max} axes are parallel to the transport direction and related to ductile S-C structures. Furthermore, the Pj-T changes across the shear zone characterize strain variations: larger Pj and T are found in the basal, most deformed part of the shear zone, and lower values are found where the interaction between Alpine and Variscan-related petrofabrics is stronger. We also interpret the reactivation of Variscan inherited fabrics within the Alpine shear zone. In spite of the heterogeneous strain, markers indicate a common, top-to-the-South (N190E) Alpine transport direction, which contrasts with the strong obliquity of the genetically-related structures developed in the Southern Mesozoic sedimentary cover. In this sense, our data suggest a complete decoupling between basement and cover units during the Alpine compression.

Keywords: shear zone, Gavarnie thrust, Pyrenees, magnetic fabrics, Alpine Orogeny

1. Introduction

In mountain belts, the majority of strain accumulated by translation of crustal volumes, both in the upper and lower crust, is partitioned and localized into narrow, discrete shear zones (e.g. Ramsay and Graham, 1970; Elliott, 1976; Sibson, 1977; Boyer and Elliott, 1982; Butler, 1987). These shear zones represent mechanically weakened portions of the crust that can be easily reactivated during subsequent deformation, controlling the tectonic evolution of plates, and especially the structure of orogens at plate margins. Therefore, the study of shear zones and specially the determination of

transport direction and strain conditions is essential to understanding the plate tectonic frame and structural evolution of orogens.

At a smaller scale, shear zones constitute domains where deformation is heterogeneous and partitioned as a result of different strain rates and/or rock strength at outcrop, sample or microscopic scales. Structural study of shear zones investigates the relationships between finite deformation patterns and strain gradients, which are usually difficult to determine or correlate. In this sense, we utilize in this work the Anisotropy of the Magnetic Susceptibility (AMS) as a useful technique in the structural analysis of shear zones because of its proved relationship with rock fabric and strain intensity (e.g. Hrouda 1987, 1993; Borradaile and Alford, 1988; Lüneburg *et al.*, 1999; Parés and van der Pluijm, 2002; Tikoff *et al.*, 2005; Ferré *et al.*, 2014 and references therein). These relationships include the correlation between the scalar parameters of magnetic ellipsoid and strain rate (e.g. Housen and van der Pluijm, 1993; Parés and van der Pluijm, 2002; Debacker et al., 2004; 2009; Haerinck *et al.*, 2013).

Furthermore, a direct relationship between the axes of the strain ellipsoid (X, Y and Z) and the axes of the magnetic ellipsoid (k_{max}, k_{int} and k_{min}, respectively) has been demonstrated (e.g. Borradaile and Tarling, 1981; Rathore et al., 1983; Borradaile, 1991). In shear zones, some of the most common kinematic indicators are lineations and S-C-C' structures (Lister and Snoke, 1984), a composite fabric resulting from the presence of shear (C-C' planes) and foliation (S) planes. Transport direction is contained on the C surfaces and is orthogonal to the intersection lineation between S and C planes. Then, magnetic lineations (k_{max}) can be either parallel (e.g. Ruf *et al.,*

1988; Zhou *et al.,* 2002; Tomezzoli *et al.,* 2003; Ferré *et al.,* 2004; Sidman *et al.,* 2005; Tikoff *et al.,* 2005; Solum and van der Pluijm*,* 2009; Ono *et al.,* 2010) or perpendicular (e.g. Parés and van der Pluijm, 2002; Mertanen and Karell, 2012; Casas-Sainz *et al.,* 2017) to the transport direction inferred from S-C structures, depending on the magnetic mineralogy, strain rate, or the slip-partitioning within the shear zone. Nevertheless, clear stretching lineations are difficult to identify in pelitic rocks with very low metamorphic grade, especially where flattening is combined with simple shear. AMS can be helpful to define the dominant set of planes in different domains of the shear zone and also to determine the mineral lineation within the rock (Debacker et al., 2009; Oliva-Urcia *et al.,* 2010; 2012a; Haerinck *et al.*, 2015).

The Gavarnie Thrust, the Pyrenean structure that is the focus of this work, is a major thrust of the west-central Axial Zone of the Pyrenees controlling a significant portion of its Cenozoic evolution. Detailed kinematic studies have not previously been carried out in this structure. For example, Grant (1989; unpublished thesis) is the only publication about this matter and only briefly documents the structural data of the shear zone developed in its hangingwall. In this work, we determine accurately the transport direction of this major structure, which is critical to understand the evolution of the Pyrenean orogen. Especially relevant is establishing the relationship between the transport direction of the thrust in the Pyrenean internal zone and the genetically related oblique structures developed in the southernmost Mesozoic sedimentary cover (Mochales et al., 2011, 2016; Muñoz et al., 2013 and references therein). The relationship between both units is a current topic in the Pyrenean studies, and several

86 questions can be put forward: Is this foreland belt related to a primarily oblique
87 transport direction of the internal zones with respect to the Pyrenean trend? Or, on
88 the other hand, does a complete decoupling exist between internal and external zones
89 favoured by the Triassic detachment level between both units? These questions are
90 important to answer and accurate determinations of transport directions based upon
91 reliable data are needed to provide these answers.

92 Fortunately, the targeted structure is characterized by outstanding exposure that
93 preserves features related to a strongly heterogeneous deformation involving different
94 strain rates and lithological changes. Therefore, it constitutes an excellent natural
95 example for analyzing the response of the magnetic fabrics to these changes. Previous
96 AMS studies dealing with composite fabrics analyse the interference of sedimentary
97 fabric (S_0) and its tectonic overprint (S_1) (Housen and van der Pluijm, 1993; Debacker et
98 al., 2004; 2009; Haerinck *et al.*, 2013), but a lacuna exists for tectonic fabrics modified,
99 reactivated or overprinted to different degrees by a second tectonic fabric, which is a
100 focus of the present contribution.

101 In summary, this work, through a detailed structural, Anisotropy of Magnetic
102 Susceptibility (AMS) and Anisotropy of the Isothermal Remanent Magnetization (AIRM)
103 study attempts to i) determine the elements that control and origin different magnetic
104 lineation (k_{max}) orientations, providing some clues about the importance of meticulous
105 studies for a correct interpretation of the magnetic lineation in heterogeneous shear
106 zones; ii) characterize qualitatively (through structural analysis) and quantitatively
107 (through the Pj-T diagram) strain histories in the Gavarnie Thrust, including a probably

local shear-reactivation of inherited Variscan petrofrabrics during Alpine deformation; and iii) obtain novel kinematic data of the Gavarnie Thrust to characterize the structure and to establish the relationships between the genetically-related internal and external zones of the Pyrenean orogeny.

2. Geological Setting

The Pyrenees are an ESE-WNW trending, Alpine chain resulting from the collision between the Iberian and European plates during Late Cretaceous to Early Miocene times (Muñoz, 1992; among others). The uplift of the Palaeozoic Axial Zone related to crustal-scale Alpine thrusts defines an antiformal stack (Fig. 1a). In the study area, this antiformal stack is composed of four thrust sheets emplaced in a piggyback sequence and named from top to bottom as Gavarnie, Millares, Bielsa and Guarga thrusts (Fig. 1b; Casas *et al.,* 2003; Martinez-Peña and Casas-Sainz, 2003; Izquierdo-Llavall *et al.,* 2015). The timing of thrust sequence has been corroborated from thermochronological analysis by Metcalf *et al.* (2009) and Rahl *et al.* (2011), indicating two phases of authigenic mineral neoformation: a main phase of high-temperature fluid migration at 70 Ma and a late low-temperature pulse at 32 Ma. The southern part of the range is a fold-and-thrust foreland belt involving a Mesozoic-Cenozoic cover, detached from the basement by the Upper Triassic evaporites (Séguret, 1972; Williams and Fischer, 1984; Muñoz *et al.,* 1986; Muñoz, 1992).

128 The Gavarnie thrust (GT) places Devonian and Silurian low-grade metasediments onto
129 Cambrian-Ordovician intermediate-grade metasediments intruded by Variscan granites
130 (Fig. 1c; Séguret, 1972; Parish, 1984; Román-Berdiel *et al.,* 2004). The Paleozoic rocks
131 in the footwall are unconformably covered by a thin, discontinuous Mesozoic cover
132 consisting of Triassic red beds and Cretaceous limestones (Oliva-Urcia *et al.*, 2012b;
133 Izquierdo-Llavall *et al.*, 2014, 2015). In the hangingwall of the GT, the Variscan foliation
134 associated with the main, south-verging, Variscan D2 phase, trends E-W to NW-SE and
135 dips N to NE (Soula et *al.*, 1986; García-Sansegundo, 1996; García-Sansegundo *et al.,*
136 2011). This Variscan foliation is nearly parallel to the E-W Alpine foliation developed in
137 the Axial and South-Pyrenean zones (Holl and Anastasio, 1995; Izquierdo-Llavall *et al.*,
138 2013). Triassic red beds are confined to small fault-bounded basins underlying the
139 Cretaceous carbonates, which are more extensive and mylonitized in the footwall of
140 the GT (Grant, 1989; 1990; de Bresser, 1989).

141 A SSW transport direction has been classically assumed for the South Pyrenean zone.
142 This transport direction fits with that observed in Alpine structures within the Gavarnie
143 hangingwall (Parish, 1984), in the Pic de Port Vieux Thrust, a second-order thrust
144 related to the GT (Grant, 1989; 1990) and also in the Monte-Perdido thrust system
145 (Fig. 12; Lacroix *et al.* 2011). Nevertheless, only in the kinematic data of Grant (1989)
146 about the Gavarnie Thrust is this assumption provided with preliminary
147 documentation. Grant (1989) also noted that the Variscan foliation was slightly rotated
148 from its regional trend (E-W) in the non-sheared hangingwall, to a NE-SW trend within
149 the Alpine shear zone. P-T conditions point to ductile deformation and shearing

150 temperatures between 250 and 300 °C inferred from deformational structures (de
151 Bresser, 1989) or fluid inclusions (McCaig *et al.,* 1995; 2000).

152 Our study is focused on the western sector of the Gavarnie thrust (Fig. 1a), at the
153 Barrosa cirque (at 2500 m height, 3 hours walk up the Barrosa Valley), where the
154 Gavarnie thrust shows a spectacular exposure of a 40 m thick shear zone, resulting
155 from the deformation of Silurian phyllites, Devonian phyllites and limestones, and
156 Cretaceous limestones, that allows for a new detailed comparison between structural
157 analysis and magnetic fabrics.

158 **3. Methodology**

159 *3.1. Structural Analysis*

160 For the detailed study of the GT-related deformed zone, 3 profiles were sampled (Fig.
161 2a, d). Along these profiles, structural data and samples for the AMS analysis were
162 collected. The first profile is parallel to the basal thrust plane (N42.71850; E0.14421 to
163 N42.72205; E0.14758), and the other two profiles (A and B) are vertical and orthogonal
164 to the plane of the shear zone (Fig. 2). Coordinates for A and B profiles are N42.71961;
165 E0.14490 to N42.71983; E0.14461 and N42.72200; E0.14873 to N42.72247; E0.14881,
166 respectively. This field-work strategy enabled us to identify if lithological changes
167 affect the orientation of the transport direction, strain distribution and the axes
168 orientation of the magnetic ellipsoid.

169 For the kinematic interpretation of the structure, outcrop-scale indicators, namely
170 foliation planes, S-C structures and their associated lineations were measured and

represented in stereoplots using the Stereonet software (Allmendinger *et al.*, 2013). The microstructural study was carried out by means of 36 thin-sections oriented parallel to the XZ (29) and YZ (7) planes of the Alpine finite strain ellipsoid, and studied under reflected and transmitted light with a petrographic microscope.

3.2. Magnetic techniques: RT-AMS, LT-AMS, AIRM

3.2.1. RT-AMS

The anisotropy of magnetic susceptibility is described by a symmetric second-rank tensor with three principal components ($k_{max} \geq k_{int} \geq k_{min}$), which can be represented by the three orthogonal axes of magnetic ellipsoid. The maximum axis (k_{max}) is defined as the magnetic lineation and the minimum axis (k_{min}) is normal to the magnetic foliation, which is defined by k_{max} and k_{int} axes. The bulk magnetic susceptibility (K_m) is the arithmetic mean of the principal susceptibilities ($K_m=1/3(k_{max}+k_{int}+k_{min})$. Relationships between these axes (normalized by means of Jelinek's method, 1977) provides the corrected anisotropy degree Pj and the shape parameter T (Jelinek, 1981):

$$\mathrm{Pj} = exp\sqrt{2[(\mu_1 - \mu_m)^2 + (\mu_2 - \mu_m)^2 + (\mu_3 - \mu_m)^2}$$

$$T = \frac{2\mu_2 - \mu_1 - \mu_3}{\mu_1 - \mu_3}$$

where μ_1, μ_2, and μ_3 represent $\ln(k_{max})$, $\ln(k_{int})$, and $\ln(k_{min})$, respectively, and $\mu_m = (\mu_1+\mu_2+\mu_3)/3$. Pj can be conditioned by the magnetic mineralogy and its degree of alignment, whereas T indicates the shape of the ellipsoid, where $0<T<1$: oblate ellipsoids and $-1<T<0$: prolate ellipsoids. Magnetic lineation ($L=(k_{max}-k_{int})/k_m$) and

foliation ($F=(k_{int}-k_{min})/k_m$) parameters are also used for the characterization of the ellipsoid. The average directional and scalar value for each site was calculated using Jelinek (1978) statistics with Anisoft 4.2 (Chadima and Jelinek, 2009).

Samples were collected from 28 sites (436 specimens) in three different ways: i) *in situ* drilling (9 sites, 124 standard cylindrical specimens of 2.5x2.1 cm) with a portable electric drill, and oriented *in situ* with an orientation device, ii) drilled from oriented hand samples (5 sites, 69 specimens) and oriented using the orientation device after setting the block in its *in situ* position, and iii) cut in cubes by means of a trim saw from oriented hand blocks (14 sites, 243 specimens of 2.1x2.1x2.1 cm) using the orientation of one of their flat surfaces. To determine the magnetic fabric orientation, which results from the contribution of all mineral phases (dia-, para- and ferromagnetic *s.l.*), specimens were measured at room temperature (RT-AMS) with a KLY-3S Kappabridge (AGICO-Advanced Geoscience Instruments Company) susceptometer, a bridge at low magnetic field (300 A/m, 875 Hz), in the Magnetic Fabrics Laboratory of the University of Zaragoza (Spain).

3.2.2. LT-AMS

The susceptibility of the paramagnetic minerals (i.e. phyllosilicates) is exponentially enhanced at low temperatures, as indicated by the Curie-Weiss law for the paramagnetic behaviour: $K_{para}=C/T-\Theta$, where K_{para} is the paramagnetic susceptibility, C is the Curie constant and Θ is the paramagnetic Curie temperature (Ihmlé *et al.*, 1989; Ritcher and van der Pluijm, 1994; Bierdemann *et al.*, 2014). To separate the paramagnetic subfabric from the total fabric, 8 sites (50 samples, 5-7 per site) were

analysed at low temperature in the KLY-3S Kappabridge (AGICO) susceptometer at the University of Zaragoza. Following previous studies (Schultz and Heller, 1985; Jover *et al.*, 1989; Oliva-Urcia *et al.*, 2009, 2010; García-Lasanta *et al.*, 2014), the LT-ASM measurement procedure is as follows: after a 1 hour cooling down at 77K by immersion in liquid nitrogen, the samples were measured in the three positions required by the apparatus, and a fourth measurement to obtain the bulk susceptibility, immersing the samples again for 10 minutes between each measurement. Thermal protection around the measuring coil is used to prevent instrument drift by the cold sample (Issachar *et al.*, 2016). A pure paramagnetic sample measured at low temperature (77K) must show an increase of its susceptibility of approximately 3.8 times with respect of its susceptibility at room temperature (Lüneburg *et al.*, 1999), whereas the presence of ferromagnetic *s.l.* minerals reduces this ratio.

3.2.3. AIRM

Anisotropy of Isothermal Remanent Magnetization (AIRM) was measured in order to determine the magnetic fabric associated to the ferromagnetic *s.l.* phases (Stephenson *et al.*, 1986; Jackson, 1991; Aubourg *et al.*, 2000; Potter, 2004; Billardelo and Jackson, 2014). For this purpose, 3-4 samples were measured in each site, selecting the samples that were previously measured for RT and LT. For the AIRM determinations, a direct field (DC) of 2T was imparted with a M2T-1 pulse magnetometer in nine different positions to each sample. The acquired magnetization was measured in a cryogenic 2G 755 magnetometer at the University of Burgos (Spain). Thus, we used the nine

233 measurements for the definition of the anisotropy tensor and the triaxial ellipsoid of
234 the AIRM, following the procedures described in Girdler (1961).

235 *3.3. Mineralogical analysis*

236 In order to determine the mineralogy of the samples, X-ray diffraction (XRD) analyses
237 were performed with a Scintag X1 X-ray system (CuKα radiation) at 40 kV and 45 mA at
238 the University of Roma Tre. For the whole rock composition, randomly oriented
239 powder samples were run in the 2°–70°2θ interval with a step size of 0.05°2θ and a
240 counting time of 3 s per step. For the clay analysis, the <2μm (equivalent spherical
241 diameter) grain-size fraction was separated by centrifugating and oriented air-dried
242 and ethylene–glycol solvated samples were scanned from 1° to 48°2θ and from 1° to
243 30°2θ, respectively, with a step size of 0.05°2θ and a count time of 4 s per step.

244 Temperature variation of magnetic susceptibility (κ-T) studies were performed from -
245 195 °C to room temperature and from room temperature to 700 °C in a KLY-3S
246 Kappabridge combined with a CS-L cryogenic apparatus and a CS-3 furnace (AGICO
247 company). The heating/cooling runs were performed on 18 samples in argon
248 atmosphere to minimize mineral reactions with oxygen during heating. The data were
249 corrected for the empty furnace with the Cureval software of AGICO (Chadima and
250 Hrouda, 2009). The presence of paramagnetic phases (phyllosilicates) induces a
251 hyperbolic shape of the curve at its lowest temperature. Sharp decreases in the
252 susceptibility indicate the Curie or Néel temperatures, which is the transition between
253 ferromagnetic *s.l.* to paramagnetic behaviour (Hrouda *et al.*, 1997).

ACCEPTED MANUSCRIPT

To determine the ferromagnetic *s.l.* phases, acquisition of Isothermal Remanent Magnetization (IRM) was performed in four samples, allowing us to identify the magnetic coercivity and the relative contribution of the different components. The samples were exposed progressively to fields up to 2T in 12 steps using a M2T-1 pulse magnetometer. To complete the determination of ferromagnetic *s.l.* phases, thermal demagnetizations of the three axis IRM were performed. Three decreasing magnetic field of 2000mT, 400mT and 120mT were applied subsequently in orthogonal directions (X, Y and Z sample position, respectively) with a M2T-1 pulse magnetometer (following Lowrie, 1990). Hence, the samples were magnetized in the three orthogonal axes according to their coercivity, and subsequently stepwise thermally demagnetized with an ASC-TD48-DC oven from room temperature to 680 °C. The remanent magnetization was measured in a cryogenic 2G 755 magnetometer. The unblocking temperature along each axis allowed us to interpret the Curie temperature of the phases present in the samples.

A Philips XL30 tungsten-filament SEM was used to obtain backscattered electron images (20kV) at the University of Liverpool to complement the information extracted from the microstructural study with the optical microscope. The semi-quantitative EDS analyses (chemical mapping and spectrums) were carried out to identify and characterize mineral composition.

4. Structural analysis

4.1. Structure of the shear zone (Strain distribution)

In the studied sector of the Barrosa outcrop (Fig. 2), the shear zone of the GT is developed in the Silurian ampelites, which acted as the main detachment level, and in the Devonian phyllites and limestones of the Fourche de la Sède Formation (Joseph and Lucas, 1972; Parish, 1984). Both formations overthrust the Permo-Triassic and Cretaceous cover and the Bielsa Granitoid (Figs. 1, 2; Casas *et al.,* 2003, Román-Berdiel *et al.,* 2004). The hangingwall contains a recumbent anticline, whose overturned southern limb is involved within the shear zone (Fig. 2c). Because of this geometry, the younger Devonian units are incorporated to the shear zone towards the South (Fig. 2a, b, c), replacing the Silurian rocks that become thinner and pinch out completely towards the south and, so that the décollement level migrates in to the Devonian phyllites and limestones.

The shear zone is a flat-lying sheet about 40 m thick and characterized by well-developed S-C structures and mylonitic foliations that gradually become less developed toward the top, with a progressive increase of the angle between S and C planes and decrease in their penetrativeness (Figs. 3, 4). The textural elements of the Variscan foliation (S_v in Fig. 3) are better preserved towards the top.

The strain distribution observed within the shear zone depends both on the distance to the thrust plane and lithology. Along profile B (Fig. 3), where only the Silurian phyllites are involved, two different zones were observed considering the intensity of Alpine deformation: i) the lower zone, characterized by S-C-C' structures; and ii) the upper zone, characterized by structures related to brittle deformation affecting the Silurian protolith, which preserves a relatively undisturbed Variscan foliation (S_v

297 foliation in Fig. 3f-j). Within the lowermost 2m of the profile a fine C-parallel foliation
298 (Fig. 3a, b) was identified and progressively increases in angle with respect to the shear
299 bands, forming clear S-C structures up to 9-10 m from the base of the zone (Fig. 3c-e).
300 Within the upper brittle zone, the Alpine-related strain is restricted to individualized
301 shear planes with Y, R and P Riedel orientations (Alpine brittle shear planes in Fig. 3g,
302 i). These planes delimit decametric to metric-scale lithons that preserve internally the
303 inherited S_v Variscan foliation (Fig. 3f-j). Although this S_v foliation predates Alpine
304 shear, it changes geometrically according to the distance to the thrust plane, showing
305 less pervasiveness and a tendency to steeper dips towards the roof (Fig. 3). Bedding
306 planes are not visible within lithons under the naked eye, most probably because it has
307 been obliterated by the S_v foliation.

308 Where both limestones and phyllites are involved (profile A, Fig. 4), the strain
309 distribution is even more heterogeneous because of the different rheology of the
310 phyllites and limestones along with the upward shift of the main décollement towards
311 the Devonian units. Within the lowermost 4m (Fig. 4a-d), the Silurian phyllites show
312 well-developed S-C structures. Upwards, around the lithological contact between
313 Silurian phyllites and Devonian phyllites and limestones, deformation is evidenced by
314 C-parallel phyllonites and mylonites (Fig. 4e, f). These structures evolve upwards to S-
315 C-C' structures (7-11m; Fig. 4g, h) and then to irregular foliation affected by brittle-
316 ductile shear bands (C' in Fig. 4 I, j). Small-scale drag folds associated with the shear
317 bands, sheath folds and coaxial, second-generation folds that deformed the pre-
318 existing foliation planes, are also present in this upper zone.

319 *4.2. Rock fabrics – Kinematic indicators (Mesoscale)*

320 Alpine foliation (S) planes show an E-W directional maximum, with a scattering that
321 reaches N-S trends (Fig. 5a), probably caused by local changes in displacement
322 direction within the shear zone and by the presence of sheath folds and N-S trending
323 folds (see Carreras *et al.*, 2005, for more details). S planes dip generally towards the N,
324 consistently with the top-to-the-S transport direction of the GT. Shear bands or C
325 planes are sub-horizontal or dip slightly (20-30°) to the North, parallel to the thrust
326 surface (Fig. 5b). The frequency of C planes decreases exponentially towards the upper
327 part of the shear zone, with spacings ranging from a few centimetres in the most
328 strained zone to 1 m where the discrete, brittle shear bands delimit lithons in profile B
329 (Fig. 3g, i). C' planes are heterogeneously distributed in the fault zone, showing
330 variable trends (from N-S to E-W), mainly dipping to the South and cutting S-C
331 structures and mylonites.

332 Stretching lineations or striations on S and C planes plunge northwards and trend
333 between N340E and N040E (average N004E, Fig. 5c). Even when cleavage strikes N-S,
334 the lineation shows an overall N trend, being the most reliable kinematic indicator at
335 the outcrop scale. These lineations are almost parallel to the transport directions
336 inferred from S-C structures, ranging between N325E and N040E, with an average in
337 N009E (Fig. 5c). These N-plunging lineations are also present on the S_v Variscan
338 foliation planes (Profile B, Fig. 3) as striations, although in a noticeably minor
339 frequency.

340 *4.3. Microstructural studies*

ACCEPTED MANUSCRIPT

341 According to the meso-scale study, S-C structures are the main feature observed in the
342 Silurian phyllites, showing a strong alignment of phyllosilicate minerals (Fig. 3b, d; Fig.
343 4b, d), arranged parallel to S, C and C' planes in the XZ section. Quartz grains are less
344 abundant than phyllosilicatesand form sigmoidal porphyroblasts parallel to the S
345 planes (Fig. 3b, d; Fig. 4b, d). Although the S and C are the most common planes of
346 anisotropy, C' planes are well developed locally and are able to control the internal
347 fabric, constituting a conspicuous third anisotropy plane (Fig. 4g). Moreover, brittle
348 fractures cut and postdate previous S-C-C' structures, being the P fracture orientation
349 the most common (Fig. 3d).

350 In the lower zone of the profile B, at the contact with the Cretaceous limestones, a C-
351 parallel foliation is consistently observed in outcrop (Fig. 3a, b), showing a strong
352 alignment of phyllosilicates and sigmoidal quartz grains in the XZ section. Upwards, S-C
353 structures in phyllosilicates are well developed and a decrease of the pervasiveness
354 and an increase of spacing of C and S planes and grain size are observed toward the
355 upper limit of the highly strained zone (8-10m) (Fig. 3c-e). In the first 10m, the YZ
356 sections show mineral grains clearly less stretched than in the XZ section, indicating no
357 strong slip-partitioning and most probably a stretching along the X strain ellipsoid.
358 From this zone up to the top of the shear zone, a pervasive pressure-solution foliation
359 (Fig. 3h, j) fits in orientation with the main S_v Variscan foliation preserved within Alpine
360 lithons and observed at outcrop scale (Fig. 3g, i). The S_v planes seem to be less
361 penetrative towards the top of the shear zone and first obliterates (Fig. 3f) and then
362 crenulates a previous anisotropy plane characterized by a horizontal mineralogical

363 banding (Fig. 3h, j), which is not usually visible at the outcrop scale (Fig. 3g, i). The
364 horizontal disposition of these planes leads us to interpret them as the horizontal
365 bedding (S_0 in Fig. 3) observed in the Barrosa Cirque (Fig. 2), although it could be also a
366 bedding-parallel Variscan foliation. The Alpine brittle shear bands observed in the field
367 are missing in thin section, most probably because their spacing is greater than the
368 width of the thin section. Mineral lineations are poorly developed in XZ and YZ sections
369 in this uppermost zone (10-37m) of the profile B, indicating less stretching than in the
370 lower 10m of the profile.

371 The Devonian calcite-rich mylonites (profile A) are characterized by the presence of a
372 parallel layering formed by bands of calcite grains, calcite mixed with fine-grained
373 phyllosilicates and phyllosilicates, that are parallel to the S or C planes at micro-scale
374 (Fig. 4f, h, j). Calcite grains show a strong shape and crystallographic preferred
375 orientation, with their long axis (X) parallel (on the C plane) or slightly oblique (on the S
376 plane) to the transport direction (into XZ section), compatible with the shear sense,
377 and most probably accommodating most of the strain (Marcén *et al.*, 2017). The
378 parallelism of this layering with respect to the shear bands (and also to each other) is
379 controlled by strain, since they are nearly parallel when approaching the thrust plane
380 (Fig. 4f) and oblique (S-parallel) towards the upper zones of the shear zone (Fig. 4h, j).
381 The presence of dark organic matter and also the fine grain-size prevents clear
382 identification of mineralogical lineations in phyllosilicates (Fig. 4f, h, j), both in XZ and
383 YZ sections. Nevertheless, calcite grains are clearly more stretched in the XZ than in YZ
384 section, indicating stretching lineation along the X strain axis.

5. Mineralogical and magnetic analysis

X-ray diffraction analyses of the whole rock composition and <2µm grain-size fraction were performed in samples from the B and A vertical profiles including both Silurian (11 samples) and Devonian (3 samples) rocks (Table 1). The Silurian phyllites are mainly composed of phyllosilicates and quartz with subordinate amounts of K-feldspar, calcite and pyrite. The Devonian mylonites contain calcite and phyllosilicates as major components, with quartz, pyrite, dolomite and K-feldspar as subordinate minerals. Ferromagnetic *s.l.* minerals are rarely observed and magnetite and pyrrhotite are present as minor components (<1 wt%). A significant increase of the amount of phyllosilicates towards the thrust plane was observed in both profiles

In the <2 µm grain size fraction, among the phyllosilicate group, muscovite, paragonite and chlorite are the major minerals indicative of low-grade mineralogical assemblages consistent with fluid-inclusion data (McCaig *et al.,* 1995; 2000). This result also fits with the first phase of authigenic mineral neoformation at 70Ma identified by Rahl *et al.* (2011). No significant changes were observed between the two dominant lithologies. Only one site (Cp7) located at the base of profile B, shows a different mineralogical association of kaolinite, talc and long-range ordered mixed-layers illite-smectite, in addition to muscovite, paragonite and chlorite (Table 1), that is interpreted to exist because the original mineralogy was greatly altered by the passage of chemically active fluids.

The 18 temperature-dependent susceptibility (k−T) curves corroborate the dominance of phyllosilicates (paramagnetic phases), since they show a hyperbolic shape at low

407 temperature and at the initial heating steps in 15 samples (Fig. 6). In all samples, an
408 increase in the susceptibility starting from 300 °C or 400 °C, the final decay at 580-600
409 °C and the non-reversibility of the curves indicate the neoformation of
410 magnetite/maghemite during heating. Minor amounts of original maghemite (Fig. 6a,
411 b) and magnetite (Fig. 6c) can be observed in 8 samples. The increase in susceptibility
412 around 300 °C suggest the presence of iron sulphides (i.e., pyrrhotite; Fig. 6a, b).

413 To resolve the ambiguity in the identification of ferromagnetic s.l. minerals from the
414 thermomagnetic curves, acquisition curves and thermal demagnetization of the three
415 axis IRM have been performed. The IRM acquisition curves show different saturation
416 magnetic fields: taking 0.2 T as reference, 57-80-91% of the IRM is saturated as shown
417 in Fig. 6d for BA17-7, BA17-1 and BA10 samples, respectively, indicating a higher
418 coercivity mineral present in the lower percentage of the saturated IRM. (Ba17-7 in
419 Fig. 6d). Thermal demagnetization of the three axis IRM is consistent with the IRM
420 acquisition curves, and indicates higher magnetizations in the axes along which the low
421 (120mT) and intermediate (400mT) fields were applied, thus indicating the presence of
422 magnetite/maghemite (Fig. 6e) and iron-sulphides (Fig. 6f) with a sharp decrease in
423 magnetization at their Curie temperatures. Hematite was not identified in the samples.

424 The semi-quantitative EDS-SEM is a powerful technique, not only to determine the
425 minerals present, but also their structural position. This analysis reveals the presence
426 of chlorite and an Al-rich and Fe-poor muscovite type, most probably phengite, as
427 phyllosilicates (Fig. 7a, b), and quartz, calcite and pyrite as the major minerals,
428 consistent with XRD analysis. As accessory minerals, iron oxides and sulphides, titanite,

chalcopyrite and phosphates were identified. Both in limestones and phyllites, phyllosilicates (not clearly visible in thin sections of the Devonian limestones, Fig. 4f, h, j) are aligned parallel to S or C planes in S-C structures (Fig. 7a) or parallel to mylonitic foliations (Fig. 7b), whereas iron oxides are present mainly as the replacement of pyrites (Fig. 7c) and also present as thin sheets parallel to S and C planes (Fig. 7a).

6. Magnetic fabrics

6.1. Scalar properties and their distribution

Mean susceptibility measured at room temperature in the Silurian specimens varies from 0.5 to 298 x 10^{-6} (SI), whereas in the Devonian phyllites and limestones the susceptibility ranges from 14 to 206 x 10^{-6} (SI) (Table 2 and Fig. 8). The distribution of susceptibility values within the shear zone is not homogeneous, and increases towards its base in both profiles (Table 2; Fig. 8a). The higher amount of phyllosilicates (Table 1) and ferromagnetic *s.l.* phases, inferred from the higher magnetizations obtained in AIRM analysis, at the base of profile B suggests a direct relationship with the bulk susceptibility.

The corrected degree of anisotropy (Pj) shows similar values in Silurian and Devonian rocks, ranging between 1.03 and 2.52 (Table 2). The highest values of Pj (>1.75) occur in samples with values of the bulk susceptibility close to zero (Ba17-6 and Ba17-10 sites, and some samples in Ba17-7 and Ba17-11), which are not represented in Fig. 8 because they are not reliable, following Hrouda (2004). Pj or T parameters do not correlate with the bulk susceptibility (Fig. 8c), suggesting that strain, and not the type

450 or amount of magnetic minerals, controls the magnetic anisotropy (Parés and van der
451 Pluijm, 2002). The analysis of the evolution along profile B of the Pj values (Fig. 8b) and
452 of the Pj-T relationship (Fig. 8d) indicate a zonation within the shear zone. The basal
453 part of the shear zone shows oblate fabrics with high Pj (Pj≈1.20) values, whereas the
454 intermediate zone show an evolution along the profile from oblate to triaxial-oblate
455 fabrics and minor Pj values (Pj≈1.10). Finally, the uppermost zone shows a progressive
456 increase with height of both T and Pj parameters, from triaxial-oblate fabrics (T=0.30;
457 Pj≈1.17, in Ba17-7) to oblate fabrics (T=0.77, Pj≈1.35, in Ba17-11, the Silurian
458 protolith). Only the Ba17-12 site does not follow this evolution and instead, shows
459 similar parameters to the Silurian protolith (Fig. 8d). These three zones fit with the
460 observed upward sequence of changes in the deformational structures (C-parallel
461 foliation, S-C structures and inherited fabrics, respectively) observed along the profile.
462 Similar parameters have been observed in profile A (Table 2), but the presence of
463 different rheologies and lithologies lead us to interpret these data with a greater
464 caution.

465

466 *6.2. AMS directional data*

467 For all sites, a good correlation exists between the observed rock fabric observed in
468 the field and thin section, and the orientation of the axes of the magnetic ellipsoid. k_{min}
469 axes coincide in all sites with the pole to foliations (S or S_v) planes, C planes or
470 mylonitic foliation planes (Figs. 9, 10), which are mainly defined by the strong
471 alignment of the basal planes of phyllosilicates (e.g. Fig. 3b, d). Nevertheless, some

ACCEPTED MANUSCRIPT

sites (i.e. Ba8 and Ba20, Fig. 9) show sub-vertical k_{min} axes that do not fit with the poles to any structural plane. The local presence of a third set of surfaces, dipping to the South and identified as C' planes (Fig. 4g), can control the internal fabric since k_{min} axes coincide with the obtuse bisector between the north-dipping S and C planes on one side and the south-dipping C' planes on the other (site Ba8, Fig. 9).

Two major groups of magnetic fabrics can be discerned from the orientation of the magnetic lineation (k_{max} axis): i) in 22 sites, k_{max} axes plunge to the north and are parallel to the stretching lineation and the transport direction inferred from S-C structures (i.e. Ba14, Ba22 sites, Fig. 9); or ii) in 6 sites, k_{max} axes are horizontal and parallel to the intersection lineation (i.e. Ba17-12, Ba17-7, Fig. 10). The distribution of the two groups is not homogenous within the shear zone because all sites collected from the horizontal basal profile (Fig. 9) and profile A (Fig. 10), with the exception of Ba11-1, correspond to the first group. Conversely, profile B (Fig. 10), which cuts across the whole sheared zone, shows a predominance of fabrics in the lower 10m where k_{max} axes are parallel to the transport direction (Cp7 to Ba17-4 sites, Fig. 10) and towards the upper part of the shear zone, a predominance of fabrics with k_{max} axes parallel to the intersection lineation (Ba17-5 to Ba17-10 sites, Fig. 10). This second fabric type is similar to that observed in the Silurian protolith (Ba17-11 site, Fig. 10, profile B).

6.3. LT-AMS data

AMS measurements at low temperature (around 77K) have been carried out in eight representative sites (51 samples), including the two main lithologies and different orientations of the RT magnetic lineation (Table 3). The K_m-LT/ K_m-RT ratio per site

494 ranges between 3.72 and 2.20 indicating a strong influence of the paramagnetic
495 behaviour (Fig. 11b). The orientation of the LT-AMS overlaps the orientation of the RT-
496 AMS in all sites (Fig. 11a). Furthermore, significant changes at LT-AMS in the scalar
497 parameters were not observed, with the exception of site Ba17-7, which shows a
498 notable increase of Pj (from 1.12 to 1.26). This site also shows an anomalous low
499 susceptibility and the lowest K_m-LT/ K_m-RT ratio (2.20). A contribution in this site from
500 small amounts of ferromagnetic minerals cannot be discounted.

501 *6.4. AIRM data*

502 Well-defined AIRM magnetic fabric show triaxial ellipsoids in the six analysed sites (Fig.
503 11a). The orientation of the k_{max} axes of the AIRM ellipsoid is consistent with the RT-
504 and LT-AMS. Scattering of the k_{min} and k_{int} axes of the AIRM in some sites (Cp7 and
505 Ba7, Fig.11a) is greater than for RT- and LT-AMS, although no girdle distributions of
506 axes are observed. A systematically larger Pj in the AIRM measurement and oblate-
507 triaxial to prolate-triaxial AIRM ellipsoids are found, in contrast with the lower Pj
508 values and oblate ellipsoid of RT- and LT-AMS measurements. These differences are
509 larger in the Silurian phyllites than in the Devonian limestones. Thin-sections
510 observations under optical and electron (SEM) microscopes are consistent with
511 ferromagnetic fabric because they reveal that ferromagnetic s.l. minerals occupy the
512 fracture porosity along S and C planes (Fig. 7a, b) or appear as replacements of pyrites
513 (Fig. 7c).

514 **7. Interpretation**

ACCEPTED MANUSCRIPT

515 *7.1. Strain distribution*

516 We interpret a heterogeneous strain across the Gavarnie Thrust defined by i)
517 decreasing strain intensity, from bottom to top, inferred from the weaker
518 development of the Alpine structures, and an increasing prevalence of the Variscan
519 foliation imprint towards the top of the shear zone (Figs. 3, 4); ii) the migration of the
520 décollement from the Silurian phyllites to the Devonian limestones (Fig. 2); and iii) the
521 rheological difference between the Silurian phyllites and the Devonian limestones (Fig.
522 4).

523 In spite of this heterogeneous deformation, all strain markers indicate a similar, top-to-
524 the-South transport direction (N190E on average) without changes between levels
525 undergoing different strain degree or showing different lithology/rheology (Fig. 5). The
526 predominance of N-plunging AMS k_{max} axes also confirms this transport direction and
527 the usefulness of the AMS method to quantify statistically the stretching directions in
528 shear zones. This transport direction fits with those inferred in previous works for
529 secondary thrusts within the Gavarnie Unit (Parish, 1984), namely the Pic de Port Vieux
530 GT's second-order thrust (Grant, 1989; 1990) and the Monte Perdido system (Lacroix
531 *et al.*, 2011).

532 P-T conditions during the orogenic stage can be at least partly constrained from
533 deformational features: for a temperature of 300 °C in a shear zone, as inferred for the
534 GT (de Bresser, 1989; McCaig et al, 2000), calcite has ductile behaviour (Verberne *et*
535 *al.*, 2015, among others) whereas phyllosilicates are in the brittle-ductile transition
536 (den Hartog *et al.*, 2012; Zhang and He, 2016). The strong shape- and

crystallographical-preferred orientation in the mylonites confirm the ductile behaviour of the calcite, whereas the presence of S-C structures in phyllosilicates fits with a ductile-brittle behaviour (den Hartog and Spiers, 2013; Lu and He, 2014; Zhang and He, 2016). Based on the strong stretching of grains and the absence of cataclastic brittle structures, calcite, usually considered as a hard mineral in relation to phyllosilicates (Giorgetti *et al.*, 2015; Smeraglia *et al.*, 2016), seems to act in this case as a soft mineral, accommodating the deformation along with phyllosilicates in the Devonian limestones of the hangingwall. This different rheological behaviour of Silurian phyllonites (brittle-ductile) and Devonian mylonitized limestones (ductile) results in the different deformational structures (S-C structures vs C-parallel mylonitic foliations, respectively) developed under similar P-T conditions in each lithology (Fig. 9b).

7.2. Contribution of different magnetic carriers to the RT-AMS

S-C-C' structures are composite fabrics (Lister and Snoke, 1984) in the sense that they consist in different grain populations with different orientations (S parallel, C parallel or C' parallel). In all AMS sites, k_{min} is parallel to the pole of S, C or C' planes measured at field or is located at the obtuse bisector between them (Fig. 10), as has been identified in previous works of shear zones (e.g. Aranguren et al., 1996; Ferre et al., 2014, and references therein). At the thin-section scale, this coincidence is also observed in the disposition of the basal planes of phyllosilicates, arranged in parallel to S, C or C' (Fig. 3, 4), and ferromagnetic s.l. minerals determined in SEM observations (Fig. 7). When k_{min} is perpendicular to one of these sets, it must reflect the magnetic

559 predominance of a grain population over the other ones, and in the case of k_{min}
560 parallel to the bisector plane, similar contributions from the S/C-parallel and C'-parallel
561 populations (Ferre at al., 2014). In the upper zone of profile B, where Variscan fabric is
562 preserved within lithons, all sites show k_{min} perpendicular to the pressure-solution S_v
563 Variscan foliation, which is also defined by phyllosilicates and opaque minerals.

564 On the other hand, in the basal thrust plane (basal profile, Fig. 9), in profile A and in
565 the lower zone of profile B (Fig. 10) k_{max} is parallel to the transport direction, inferred
566 from stretching lineations or S-C structures, and also fits with the stronger alignment
567 of phyllosilicates in the XZ section vs. the YZ section in the Silurian phyllites. The
568 Devonian limestones and phyllites (Fig. 4) show at the microscale, opaque
569 phyllosilicates because of their small grain-size and the presence of dark organic
570 matter. Yet, the presence of calcite porphyroblasts, clear stretching lineations in calcite
571 grains and pressure shadows in pyrites indicate simple shear parallel to the XZ plane,
572 which also fits with the N-plunging k_{max} orientation in these samples.

573 In the upper zone of the profile B, mineral lineations are poorly developed and not
574 easily identified in XZ or YZ sections. In this zone, k_{max} shows a predominance of E-W
575 trends, perpendicular to the Alpine transport direction. In these samples, Alpine brittle
576 shear bands are poorly developed and do not modify significantly the orientation of
577 the textural elements of the S_v fabric at thin-section scale. Thus, they probably have no
578 influence in the magnetic fabric orientation. Therefore, we interpret these E-W
579 magnetic lineations as an intersection lineation between the more penetrative S_v and
580 more spaced S_0 Variscan anisotropy planes. This interpretation is supported by the

ACCEPTED MANUSCRIPT

similar orientation of the k_{max} obtained in the Silurian photolith (Ba17-11 in Fig. 10). In this sense, AMS method demonstrates that is as a powerful technique for identifying and quantifying petrofabric domains (e.g. S-parallel vs C-parallel or shear-related vs Variscan-inherited mineral lineations) within heterogeneous shear zones.

Magnetic subfabric separation (low temperature –LT-AMS and AIRM methods) has been performed to determine the mineral phases that control the orientation of the RT-AMS ellipsoids. Remarkably, the orientation of the LT-AMS and AIRM axes overlap the RT-AMS ellipsoids in all sites (Fig. 11a), independently of the different relationships between LT-AMS and the petrofabric. This outcome indicates that the paramagnetic and ferromagnetic *s.l.* phases contribute in the same way to the orientation of the RT-AMS. Nevertheless, the high K_m-LT/ K_m-RT ratios observed and the different Pj and T values obtained at the AIRM measurements, in relation to the ones obtained at AMS measurements, suggest a predominant contribution of the paramagnetic phases over the ferromagnetic phases to the total RT-AMS (Lüneburg *et al.,* 1999; Oliva-Urcia *et al.,* 2009; Pueyo-Anchuela *et al.*, 2012). These interpretations are supported by the low susceptibility of the samples, which fit within the typical paramagnetic range (Rochette et al., 1992; Martín-Hernández and Hirt, 2003), the high content of paramagnetic minerals (mainly phyllosilicates) revealed by XRD analysis (Table 1), and the dominance of hyperbolic shapes at first stages in thermomagnetic curves (Fig. 6).

Moreover, small amounts of subordinate ferromagnetic minerals, especially when magnetite is present, can introduce strong changes in the corrected degree of anisotropy (Pj), even if they are not influencing the ellipsoid orientation (Borradaile,

603 1988; Rochette *et al.*, 1992; Martín-Hernández and Hirt, 2003; Debacker *et al.,* 2004).
604 Nevertheless, the lack of correlation between Pj parameter with respect to the bulk
605 susceptibility at sample scale (Fig. 8c) suggest that the presence of subordinate
606 ferromagnetic minerals are not critically influencing the scalar parameters or the
607 magnetic fabric at room temperature for our samples.

608 *7.3. On the origin and evolution of foliation*

609 One of the critical points of this structural study is to recognize the imprint of the
610 Alpine shear onto the previous Variscan petro-fabric, or, in other words, to determine
611 how the Variscan petrofabric influences the strain development in this Alpine shear
612 zone. The detailed structural analysis in the field and in thin sections indicates a
613 change in the deformational conditions along the profile B (Fig. 3). Within the first 10
614 m, brittle-ductile behaviour fits with the presence of well-developed Alpine S-C
615 structures and upwards, the Alpine imprint becomes brittle structures, preserving the
616 S_v Variscan fabric within metric-scale lithons. The dip angle of the S_v planes changes
617 between different lithons, indicating a mechanism of rigid-block rotations within the
618 Alpine shear zone. Furthermore, the bimodal distribution of k_{max} axes (parallel to the
619 transport direction and parallel to intersection lineations between the Variscan S_v and
620 S_0 planes) along profile B also fits with these two structural zones.

621 Although the main Variscan S_v fabric is clearly inherited from the protolith, its
622 penetrativeness increases towards the most-strained Alpine shear zone, based on field
623 and microstructural observations (Fig. 3, f, h, j), suggesting that it could have been
624 shear-reactivated, and also rotated, during the Cenozoic deformation. A similar

situation is identified in profile A, where the same foliation observed in the Devonian protolith, consisting of dark calcite and phyllosilicate parallel layers, is also present within the Alpine shear zone with better development and stronger parallelism towards the basal thrust plane (Fig. 4f, h, j).

Two questions arise about the usefulness of AMS in this work: i) Is AMS able to provide information (beyond the clear changes in k_{max} orientation) about strain degree within the ductile sheared zone; and ii) was the Variscan S_v foliation actually reactivated within the shear zone during Alpine deformation?. Since values of Pj and T are controlled by the shape anisotropy of phyllosilicates, and not so much by ferromagnetic s.l. minerals, they can be interpreted in terms of the intensity of preferred orientation, following previous works (Housen et al. 1993; Parés and van der Pluijm, 2002; Debacker et al., 2004; 2009; Haerinck *et al.*, 2013). The novelty of our work resides in the overprinting of two strong tectonics fabrics, rather than the more typical case of a sedimentary fabric (S_0) overprinted tectonically (S_1). For this purpose, only profile B will be analysed because of its homogeneous lithology/rheology and the paramagnetic behaviour, two conditions that profile A does not completely satisfy.

The observed evolution of Pj values and Pj-T relationship vs height along profile B (Fig. 8b, d) suggests the presence of two strong fabrics, both characterized by oblate ellipsoids and values of Pj≈1.20-1.30, in the lowermost (0-2m; Cp7 and Ba17-1 sites) and uppermost (37m, within the protolith; Ba17-11 site) zones. As previously noted, the geometric relationships between AMS and petrofabrics patterns reveal their Alpine shear or Variscan inherited origin, respectively. Between both ends of the profile (2-

647 23m), triaxial-oblate ellipsoids and lower Pj values (≈1.10) were observed. This
648 intermediate zone is interpreted as the link area between the fabrics developed at the
649 boundaries of the zone.

650 Within the Alpine ductile zone (0-11m), the first 2 m (Cp7 and Ba17-1 sites) are
651 characterized by an Alpine C-parallel foliation (Pj≈1.20; T≈0.8; Fig. 8d), whereas in the
652 2-11m interval (Cp8, Ba17-4 sites), the petrofabric is clearly related to Alpine S-C
653 structures (Pj≈1.10; T varies from 0.8 to 0; Fig. 8d). The lower Pj and T values in the 2-
654 11m section are interpreted as a minor strain and preferred orientation in composite
655 S-C fabrics rather than the "single" C-parallel foliation, which is in agreement with
656 microstructural observations.

657 Upwards, within the Alpine brittle zone (11-23m), the Variscan S_v textural elements are
658 dominant at micro-scale (Fig. 3f-j), and a progressive increase of Pj and T up to the
659 protolith is noted, indicating weaker preferred orientation of phyllosilicates at the base
660 of this zone (13m; Ba17-5 site) and a progressive increase towards the upper zone
661 (Ba17-12, -7, -9 sites). The evolution observed in Fig. 8d shows a certain parallelism
662 with the classical Pj-T evolution with progressive strain in pelitic rocks proposed,
663 among others, in Parés and van der Pluijm (2004). In this model, lower Pj and T values
664 fit with the change from a sedimentary to a tectonic magnetic fabric, where the
665 interaction of the two anisotropy planes that define a composite fabric is stronger. Our
666 results indicate that the lower Pj and T values (Ba17-5 site; Fig. 8d) in the brittle zone
667 (11-23m) occur where the Variscan S_v fabric seems to be modified and reactivated by

668 the Alpine shear, in function of its higher penetrativeness than in the upper zones of
669 the profile (Fig. 3f-j).

670 Therefore, the combination of structural and AMS studies lead us to interpret a strain
671 gradient along profile B and most probably the shear-reactivation of the Variscan S_v
672 foliations during the Cenozoic compression. This interpretation is supported by the
673 parallelism between Variscan and Alpine petrofabrics, which could be favoured by
674 rotation of S_v, and also by the presence of N-plunging lineations on the Variscan S_v
675 planes in the brittle zone. In terms of petrofabric, these data indicate that the
676 reactivation of the foliation does not imply stronger preferred orientation of
677 phyllosilicates, reflected in the lower Pj observed in the intermediate zone. In this
678 sense, the Alpine shear is characterized by a strong simple shear component, as the
679 presence of S-C structures or pressure shadows around pyrites indicates, whereas the
680 absence of clear mineral lineations associated with the Variscan foliations indicates
681 dominant pure-simple shear process (flattening) during the Variscan deformation.
682 Therefore, the overprint of subsequent tectonic events by different deformational
683 processes, cannot be considered as a sum of a progressive sequence of infinitesimal
684 strains creating a stronger preferred orientation of the fabric elements. Indeed, our
685 data and analysis indicate a reduction in the preferred orientation (based on a
686 decrease of the Pj value) for the phyllosilicates where two different deformational
687 events or petrofabrics interacted in the same rock volume.

688 *7.4. Implications for Pyrenean tectonics*

ACCEPTED MANUSCRIPT

689 An overall southwards transport direction has been classically assumed for the South
690 Pyrenean zone, even in the absence of kinematic indicators for most of the thrust
691 sheets, either from the Axial Zone (basement thrust sheets) or the South Pyrenean
692 Zone (cover thrust sheets, Muñoz, 1992 and references therein). Consequently, our
693 direct measurements of kinematic indicators in the GT provide valuable inputs for
694 interpreting the Pyrenean orogeny and its evolution through time (e.g. Rosenbaum et
695 al., 2002), particularly when this kind of indicators is not available in other thrust
696 zones. One of our main results is the relatively simple kinematics preserved in the GT
697 based on: i) the constancy in the transport direction, both along and across the
698 sheared zone, from different indicators, including petrofabrics and AMS; and ii) the
699 concentration of its displacement in a relatively narrow band (up to tens of meters
700 thick. Also, the low obliquity of the transport direction with respect to the overall
701 mapped trace of the GT is remarkable, which is inferred from the E-W attitude of
702 Mesozoic beds undetached from the basement in its main hangingwall anticline
703 (Parish, 1987; Martínez-Peña and Casas-Sainz, 2003; Casas and Pardo, 2004).

704 The N185E-N200E top-to-the-south transport direction can be interpreted as the result
705 of frontal thrusting during the period of activity of the GT (Mid-Eocene according to
706 Muñoz et al., 2013; Late Eocene-Oligocene following Teixell, 1998; Latest Eocene from
707 absolute dating of illite for its youngest movements, according to Rahl et al., 2011).
708 This interpretation is corroborated by the perpendicularity of the transport direction
709 to the regional Pyrenean cleavage (and to its associated intersection lineation),
710 developed in Cretaceous to Lower Eocene rocks of the Southern Pyrenean Zone

(Schellart, 2002; Casas et al., 2003; Izquierdo-Llavall et al., 2015). As stated before, Variscan foliations were locally re-activated during the Cenozoic compression, thus contributing to the overall shortening of the Axial Zone (Mirousse and Barrère, 1993), considering the parallelism between Variscan and Alpine structures in some areas (Cochelin et al., 2017).

The Gavarnie thrust, located in the Paleozoic basement, must be genetically related to the shortening structures developed contemporarily in the Mesozoic-Cenozoic sedimentary cover overlying the Triassic detachment level (Fig. 12). Some of these structures, namely the Boltaña and Mediano anticlines (Fig. 12), are strongly oblique to the mean Pyrenean trend being at an angle of only 20° to 30° (Muñoz et al., 2013) with the transport direction obtained for the GT. This is also consistent with the strong vertical-axis rotations observed from paleomagnetic analysis in these N-S folds (Boltaña and Mediano anticlines, Mochales et al., 2011, 2016; Muñoz et al., 2013 and references therein). The evolution of N-S folds would then be inferred to result from cover kinematics only, and a complete decoupling between basement and cover must exist.

Our data related to the structures in the shear zone of the GT support an interpretation where non-rotational kinematics occurred for both of the Gavarnie unit and the underlying basement thrust sheets (from bottom to top, Guarga, Bielsa and Millares units; Martínez-Peña and Casas-Sainz, 2003; Casas et al., 2003). In fact, basement-related clockwise rotation of the basement thrusts (including the GT) would be reflected in a clockwise rotation of the transport direction according to a piggyback

733 basement thrust sequence (see Izquierdo-Llavall et al., 2018, where a moderate
734 clockwise rotation of basement thrust sheets is proposed). Changes in the direction of
735 kinematic indicators (namely AMS related to folding) have been also obtained in other
736 areas of the South-Pyrenean Zone (Pueyo-Anchuela et al., 2012; see also Oliva-Urcia et
737 al., 2009; Pocoví et al., 2014). An alternative explanation for the constancy and
738 consistency in the transport direction obtained for the GT is that different, opposite
739 rotations (counter-clockwise and clockwise rotations) of different thrust sheets
740 underlying the GT could sum up to finally obtain the SSW transport direction (this is
741 suggested, for example, in Izquierdo-Llavall et al. 2015). The diachronous evolution of
742 these different sheets would contribute to a final finite transport direction that
743 averages the previous movements. Further paleomagnetic work would be needed to
744 confirm this hypothesis.

745 **8. Conclusions**

746 In this work, we combine structural, mineralogical and magnetic data to characterize
747 the kinematics and structure of one of the most important Alpine structure in the Axial
748 Zone, Pyrenees: the Gavarnie Thrust. The detailed, integrated study provides some
749 clues about the heterogeneous strain distribution registered in the shear zone and
750 factors involved: i) a strain gradient with greater deformation towards the thrust
751 plane; ii) the detachment migration towards the Devonian formations; iii) the different
752 rheology of the involved lithologies; and iv) the inherited (and most probably
753 reactivated) Variscan fabrics. In spite of this heterogeneous deformation, strain

ACCEPTED MANUSCRIPT

754 markers indicate a constant, top-to-the-SSW (average of N010E) transport direction for
755 the Gavarnie Thrust.

756 This work shows the utility of AMS for studying complex heterogeneous shear zones
757 through changes associated with strain in the magnetic ellipsoid orientation and
758 magnitude of the scalar parameters. Magnetic lineation (k_{max}) orientations parallel to
759 the transport direction are directly related to Alpine ductile deformational structures
760 (mainly S-C structures and C-parallel mylonitic foliations), whereas k_{max} parallel to the
761 intersection lineation are inherited from the protolith (intersection between bedding
762 and Variscan foliation) and undisturbed by Alpine brittle structures. Furthermore,
763 variations in the magnitude of scalar parameters Pj and T are interpreted in relation
764 with variations in the Alpine strain across the shear zone: larger values of Pj and T are
765 present where Alpine deformation are qualitatively greater. Smaller values coincide
766 with zones where Alpine deformation reorients and most probably shear-deformation
767 reactivates coaxial, inherited Variscan foliations.

768 Finally, the SSW transport direction inferred from structural analysis and k_{max}
769 orientations are parallel to the Alpine regional shortening direction, suggesting that
770 the Gavarnie Unit did not rotate during Alpine compression. Furthermore, the
771 transport direction of the Gavarnie Thrust contrasts with the strong obliquity of the
772 genetically-related structures developed in the southern fold-and-thrust foreland belt
773 (e.g. Mediano or Boltaña anticlines). Our results suggest that a strong decoupling
774 between the Internal (Axial Zone) and External (South Pyrenean Zone) areas occurred,

775 and was favoured by the presence of Triassic, evaporitic, detachment levels in the
776 External areas.

777

778 **Acknowledgements**

779 The authors acknowledge the careful and constructive revisions from Manish A.
780 Mamtani and an anonymous reviewer, who helped to strongly improve a former
781 version of the manuscript. The authors thank Elisabetta Mariani for her help in the
782 SEM study. Cristina García-Lasanta, Pablo Calvín and Juanjo Villalaín are acknowledged
783 for their support in rock magnetism procedures and AIRM measurement. Pablo
784 Santolaria, Bennacer Moussaid and TrekkingMule Company helped in field campaigns.
785 Sveva Corrado is acknowledged for the use of the ALBA academic lab. Authors are
786 grateful to the Servicio General de Apoyo a la Investigación-SAI (Servicio de
787 Preparación de Rocas y Materiales Duros and Servicio de Líquidos Criogénicos) of the
788 University of Zaragoza. Financial support was granted by research project CGL2013-
789 42670-P and BES-2014-070167 of the MINECO (Ministerio de Economía y
790 Competitividad of Spain).

791 **References**

792 Allmendinger, R.W., Cardozo, N.C., Fisher, D., 2013. Structural Geology Algorithms:
793 Vectors & Tensors, Cambridge Univ. Press, 289 pp.

ACCEPTED MANUSCRIPT

794 Aranguren, A., Tubía, J.M., Bouchez, J.L., Vigneresse, J.L., 1996. The Guitiriz granite,
795 Variscan belt of northern Spain: extension-controlled emplacement of magma
796 during tectonic escape. Earth and Planetary Science Letters 139, 165–176.

797 Aubourg, C., Hebert, R., Jolivet, L., Cartayrade, G., 2000. The magnetic fabric of
798 metasediments in a detachment shear zone: The example of Tinos Island (Greece).
799 Tectonophysics 321, 219–236. https://doi.org/10.1016/S0040-1951(00)00049-4

800 Biedermann, A.R., Bender Koch, C., Lorenz, W.E.A., Hirt, A.M., 2014. Low-
801 temperature magnetic anisotropy in micas and chlorite. Tectonophysics 629, 63–
802 74. https://doi.org/10.1016/j.tecto.2014.01.015

803 Bilardello, D., Jackson, M.J., 2014. A comparative study of magnetic anisotropy
804 measurement techniques in relation to rock-magnetic properties. Tectonophysics
805 629, 39–54. https://doi.org/10.1016/j.tecto.2014.01.026

806 Borradaile, G.J. and Alford, C., 1988. Experimental shear zones and magnetic fabrics.
807 *Journal of structural geology*, *10*(8), pp.895–904.

808 Borradaile, G.J., 1988. Magnetic-susceptibility, petrofabrics and strain. Tectonophysics
809 156, 1–20. https://doi.org/10.1016/0040-1951(88)90279-x

810 Borradaile, G.J., 1991. Correlation of Strain with Anisotropy of Magnetic-Susceptibility
811 (Ams). Pure and Applied Geophysics 135, 15–29.
812 https://doi.org/10.1007/bf00877006

ACCEPTED MANUSCRIPT

813 Borradaile, G.J., Tarling, D.H., 1981. The influence of deformation mechanisms on
814 magnetic fabrics in weahly deformed rocks. Tectonophysics 77, 151–168.
815 https://doi.org/10.1016/0040-1951(81)90165-7

816 Boyer, S.E., Elliott, D., 1982. Thrust systems. American Association of Petroleum
817 Geologists Bulletin 66, 1196–1230. https://doi.org/10.1306/03B5A77D-16D1-
818 11D7-8645000102C1865D

819 Butler, R.W.H., 1987. Thrust sequences. Journal of the Geological Society 144, 619–
820 634. https://doi.org/10.1144/gsjgs.144.4.0619

821 Cardozo, N., Allmendinger, R. W. (2013). Spherical projections with OSXStereonet.
822 Computers & Geosciences, 51(0), 193–205.

823 Carreras, J., Druguet, E., Griera, A., 2005. Shear zone-related folds. Journal of
824 Structural Geology 27, 1229–1251. https://doi.org/10.1016/j.jsg.2004.08.004

825 Casas, A.M., Oliva, B., Román-Berdiel, T., Pueyo, E., 2003. Basement deformation:
826 Tertiary folding and fracturing of the Variscan Bielsa granite (Axial zone, central
827 Pyrenees). Geodinamica Acta 16, 99–
828 117.https://doi.org/10.1016/j.geoact.2003.09.001

829 Casas, A.M., Pardo, G., 2004. Estructura pirenaica y evolución de las cuencas
830 sedimentarias en la transversal Huesca–Oloron. In: Colombo, F., Liesa, C.L.,
831 Meléndez, G., Pocovi, A., Sancho, C., Soria, A.R. (Eds.), Itinerarios geológicos
832 por Aragón. Geo Guías (Sociedad Geológica de España), 1. ISBN: 84-930160-2-0,
833 pp. 63–96.

834 Casas-Sainz, A.M., Román-Berdiel, T., Oliva-Urcia, B., García-Lasanta, C., Villalaín,
835 J.J., Aldega, L., Corrado, S., Caricchi, C., Invernizzi, C., Osácar, M.C., 2017.
836 Multidisciplinary approach to constrain kinematics of fault zones at shallow
837 depths: a case study from the Cameros–Demanda thrust (North Spain),
838 International Journal of Earth Sciences. Springer Berlin Heidelberg.
839 https://doi.org/10.1007/s00531-016-1349-5

840 Chadima, M., Hrouda, F., 2009. Cureval 8.0: Thermomagnetic curve browser for
841 windows. Agico, Inc.

842 Chadima, M., Jelinek, V., 2009. Anisoft 4.2: Anisotropy Data Browser for Windows.
843 Agico, Inc.

844 Cochelin, B., Lemirre, B., Denèle, Y., De Saint Blanquat, M., Lahfid, A., Duchêne, S.,
845 2017. Structural inheritance in the Central Pyrenees : the Variscan to Alpine
846 tectonometamorphic evolution of the Axial Zone. Journal of the Geological
847 Society 16p.

848 de Bresser J.H.P., (1989) Calcite c-axis textures along the Gavarnie thrust zone, central
849 Pyrenees. Geol Mijnb 68: 367–376.

850 Debacker, T.N., Hirt, A.M., Sintubin, M., Robion, P., 2009. Differences between
851 magnetic and mineral fabrics in low-grade, cleaved siliciclastic pelites: A case
852 study from the Anglo-Brabant Deformation Belt (Belgium). Tectonophysics 466,
853 32–46. https://doi.org/10.1016/j.tecto.2008.09.039

ACCEPTED MANUSCRIPT

854 Debacker, T.N., Robion, P., Sintubin, M., 2004. The anisotropy of magnetic
855 susceptibility (AMS) in low-grade, cleaved pelitic rocks: influence of
856 cleavage/bedding angle and type and relative orientation of magnetic carriers.
857 Geological Society, London, Special Publications 238, 77–107.
858 https://doi.org/10.1144/gsl.sp.2004.238.01.08

859 Den Hartog, S.A.M., Spiers, C.J., 2013. Influence of subduction zone conditions and
860 gouge composition on frictional slip stability of megathrust faults. Tectonophysics
861 600, 75–90. https://doi.org/10.1016/j.tecto.2012.11.006

862 Den Hartog, S.A.M., Niemeijer, A.R., Spiers, C.J., 2013. Friction on subduction
863 megathrust faults: Beyond the illite-muscovite transition. Earth and Planetary
864 Science Letters 373, 8–19. https://doi.org/10.1016/j.epsl.2013.04.036

865 Elliott, D., 1976. The Energy Balance and Deformation Mechanisms of Thrust Sheets.
866 Philosophical Transactions of the Royal Society A: Mathematical, Physical and
867 Engineering Sciences 283, 289–312. https://doi.org/10.1098/rsta.1976.0086

868 Ferré, E.C., Gébelin, A., Till, J.L., Sassier, C., Burmeister, K.C., 2014. Deformation and
869 magnetic fabrics in ductile shear zones: A review. Tectonophysics 629, 179–188.
870 https://doi.org/10.1016/j.tecto.2014.04.008

871 Ferré, E.C., Martín-Hernández, F., Teyssier, C., Jackson, M., 2004. Paramagnetic and
872 ferromagnetic anisotropy of magnetic susceptibility in migmatites: Measurements
873 in high and low fields and kinematic implications. Geophysical Journal
874 International 157, 1119–1129. https://doi.org/10.1111/j.1365-246X.2004.02294.x

ACCEPTED MANUSCRIPT

García-Lasanta, C., Oliva-Urcia, B., Román-Berdiel, T., Casas, A.M., Hirt, A.M., 2014. Understanding the Mesozoic kinematic evolution in the Cameros basin (Iberian Range, NE Spain) from magnetic subfabrics and mesostructures. Journal of Structural Geology 66, 84–101. https://doi.org/10.1016/j.jsg.2014.05.013

García-Sansegundo, J., 1996. Hercynian structure of the Axial Zone of the Pyrenees: The Aran Valley cross-section (Spain-France). Journal of Structural Geology 18, 1315–1325. https://doi.org/10.1016/S0191-8141(96)00050-8

García-Sansegundo, J., Poblet, J., Alonso, J.L., Clariana, P., 2011. Hinterland-foreland zonation of the Variscan orogen in the Central Pyrenees: comparison with the northern part of the Iberian Variscan Massif. Geological Society, London, Special Publications 349, 169–184. https://doi.org/10.1144/SP349.9

Giorgetti, C., Carpenter, B.M., Collettini, C., 2015. Frictional behavior of talc-calcite mixtures. Journal of Geophysical Research B: Solid Earth 120, 6614–6633. https://doi.org/10.1002/2015JB011970

Girdler, R.W., 1961. The measurement and computation of anisotropy of magnetic susceptibility in rocks. Geophys. J. R. Astron. Soc. 5, 34–44.

Grant, N. T., 1989. Deformation and fluid processes in thrust sheets from the central Pyrenees. Unpublished Ph.D. thesis, University of Leeds.

Grant, N.T., 1990. Episodic discrete and distributed deformation: consequences and controls in a thrust culmination from the central Pyrenees. Journal of Structural Geology 12, 835–850. https://doi.org/10.1016/0191-8141(90)90058-7

Haerinck, T., Adriaens, R., Debacker, T.N., Hirt, A.M., Sintubin, M., 2013. Paramagnetic metamorphic mineral assemblages controlling AMS in low-grade deformed metasediments and the implications with respect to the use of AMS as a strain marker. Journal of the Geological Society 170, 263–280. https://doi.org/10.1144/jgs2012-062

Haerinck, T., Wenk, H.R., Debacker, T.N., Sintubin, M., 2015. Preferred mineral orientation of a chloritoid-bearing slate in relation to its magnetic fabric. Journal of Structural Geology 71, 125–135. https://doi.org/10.1016/j.jsg.2014.09.013

Holl, J.E., Anastasio, D.J., 1995. Cleavage development within a foreland fold and thrust belt, southern Pyrenees, Spain. Journal of Structural Geology 17, 357–369. https://doi.org/10.1016/0191-8141(94)00062-5

Housen, B.A., Richter, C., van der Pluijm, B.A., 1993. Composite magnetic anisotropy fabrics: experiments, numerical models and implications for the quantification of rock fabrics. Tectonophysics 220, 1–12. https://doi.org/10.1016/0040-1951(93)90219-A

Hrouda, F., 1987. Mathematical model relationship between the paramagnetic anisotropy and strain in slates. Tectonophysics 142, 323–327. https://doi.org/10.1016/0040-1951(87)90131-4

Hrouda, F., 1993. Theoretical models of magnetic anisotropy to strain relationship revisited. Physics of the Earth and Planetary Interiors 77, 237–249. https://doi.org/10.1016/0031-9201(93)90101-E

Hrouda, F., 2004. Problems in interpreting AMS parameters in diamagnetic rocks. Geological Society, London, Special Publications 238, 49–59. https://doi.org/10.1144/GSL.SP.2004.238.01.05

Hrouda, F., Jelinek, V., Zapletal, K., 1997. Refined techinque for susceptibility resolution into ferromagnetic and paramagnetic components based on susceptibility temperature-variation measurement. Geophysical Journal International 129, 715–719.

Ihmlé, P.F., Hirt, A.M., Lowrie, W., Dietrich, D., 1989. Inverse fabric in deformed limestones of the Morcles Nappe, Switzerland. Geophysical Research Letters 16, 1383–1386.

Issachar, R., Levi, T., Lyakhovsky, V., Marco, S., Weinberger, R., 2016. Improving themethod of low-temperature anisotropy of magnetic susceptibility (LT-AMS) measurements in air. Geochemistry, Geophysics, Geosystems 2940–2950. https://doi.org/10.1002/2016GC006339.Received

Izquierdo-Llavall, E., Aldega, L., Cantarelli, V., Corrado, S., Gil-Peña, I., Invernizzi, C., Casas, A.M., 2013. On the origin of cleavage in the Central Pyrenees: Structural and paleo-thermal study. Tectonophysics 608, 303–318. https://doi.org/10.1016/j.tecto.2013.09.027

Izquierdo-Llavall, E., Casas-Sainz, A., Oliva-Urcia, B., Scholger, R., 2014. Palaeomagnetism and magnetic fabrics of the Late Palaeozoic volcanism in the Castejón-Laspaúles basin (Central Pyrenees). Implications for palaeoflow

938 directions and basin configuration. Geological Magazine 151, 777–797.
939 https://doi.org/10.1017/S0016756813000769

940 Izquierdo-Llavall, E., Casas Sainz, A., Oliva-Urcia, B., Burmester, R., Pueyo, E.L.,
941 Housen, B., 2015. Multi-episodic remagnetization related to deformation in the
942 Pyrenean Internal Sierras. Geophysical Journal International 201, 891–914.
943 https://doi.org/10.1093/gji/ggv042

944 Izquierdo-Llavall, E., Casas-Sainz, A.M., Oliva-Urcia, B., Villalín, J.J., Pueyo, E.,
945 Scholger, R., 2018. Rotational kinematics of basement antiformal stacks:
946 paleomagnetic study of the western Nogueras Zone (western Pyrenees). Tectonics,
947 https://doi.org/10.1029/2018TC005153

948 Jackson, M., Tauxe, L., 1991. Anisotropy of magnetic susceptibility and remanence:
949 developments in the characterization of tectonic, sedimentary, and igneous fabric,
950 Rev. Geophys., 29, 371–376.

951 Jelinek, V., 1977. The statistical theory of measuring anisotropy of magnetic
952 susceptibility of rocks and its application. GeofIz. Brno 87.

953 Jelínek, V., 1978. Statistical processing of anisotropy of magnetic susceptibility
954 measures on groups of specimens. Studia geophisica et geodetica 22, 50–62.

955 Jelinek, V., 1981. Characterization of the magnetic fabric of rocks. Tectonophysics 79,
956 63–67.

ACCEPTED MANUSCRIPT

957 Joseph, J., Lucas, C., 1972. Deformation Hercyniennes et Pyrenees dans la nappe de
958 Gavarnie. C.r. hebd. Séanc. Acad. Sci., Paris 276, 3107–3110.

959 Jover, O., Rochette, P., Lorand, J.P., Maeder, M., Bouchez, J.L., 1989. Magnetic
960 mineralogy of some granites from the French Massif Central: origin of their low-
961 field susceptibility. Physics of the Earth and Planetary Interiors 55, 79–92.
962 https://doi.org/10.1016/0031-9201(89)90235-5

963 Lacroix, B., Buatier, M., Labaume, P., Travé, A., Dubois, M., Charpentier, D.,
964 Ventalon, S., Convert-Gaubier, D., 2011. Microtectonic and geochemical
965 characterization of thrusting in a foreland basin: Example of the South-Pyrenean
966 orogenic wedge (Spain). Journal of Structural Geology 33, 1359–1377.
967 https://doi.org/10.1016/j.jsg.2011.06.006

968 Lister, G.S., Snoke, A.W., 1984. S-C Mylonites. Journal of Structural Geology 6, 617–
969 638.

970 Lowrie, W., 1990. Identification of ferromagnetic minerals in a rock by coercivity and
971 unblocking temperature properties. Geophysical Research Letters 17 (2), 159–162

972 Lu, Z., He, C., 2014. Frictional behavior of simulated biotite fault gouge under
973 hydrothermal conditions. Tectonophysics 622, 62–80.
974 https://doi.org/10.1016/j.tecto.2014.03.002

975 Lüneburg, C.M., Lampert, S. a., Lebit, H.D., Hirt, A.M., Casey, M., Lowrie, W., 1999.
976 Magnetic anisotropy, rock fabrics and finite strain in deformed sediments of SW

977 Sardinia (Italy). Tectonophysics 307, 51–74. https://doi.org/10.1016/S0040-
978 1951(99)00118-3

979 Marcén, M., Román-Berdiel, T., Marianni, E., 2017. Registro de la deformación a
980 escala microestructural en el cabalgamiento de Gavarnie (Zona Axial Pirenaica).
981 Geogaceta, 61, 99–102.

982 Martínez-Peña, M. B., and A. M. Casas-Sainz (2003), Cretaceous-tertiary tectonic
983 inversion of the Cotiella Basin (southern Pyrenees, Spain), Int. J. Earth Sci., 92,99–
984 113.

985 Martín-Hernández, F., Hirt, A.M., 2003. The anisotropy of magnetic susceptibility in
986 biotite, muscovite and chlorite single crystals. Tectonophysics 367, 13–28.
987 https://doi.org/10.1016/S0040-1951(03)00127-6

988 McCaig, A.M., Wayne, D.M., Marshall, J.D., Banks, D., Henderson, I., 1995. Isotopic
989 and fluid inclusion studies of fluid movement along the Gavarnie Thrust, central
990 Pyrenees; reaction fronts in carbonate mylonites. American Journal of Science 295
991 (3), 309–343.

992 McCaig, A.M., Tritlla, J., Banks, D.A., 2000. Fluid flow patterns during Pyrenean
993 thrusting. Journal of Geochemical Exploration 69–70, 539–543.
994 https://doi.org/10.1016/S0375-6742(00)00060-1

995 Mertanen, S., Karell, F., 2012. Palaeomagnetic and AMS studies on Satulinmäki and
996 Koijärvi fault and shear zones. Special Paper of the Geological Survey of Finland
997 2012, 195–226.

998 Metcalf, J.R., Fitzgerald, P.G., Baldwin, S.L., Muñoz, J.A., 2009. Thermochronology of
999 a convergent orogen: Constraints on the timing of thrust faulting and subsequent
1000 exhumation of the Maladeta Pluton in the Central Pyrenean Axial Zone. Earth and
1001 Planetary Science Letters 287, 488–503. https://doi.org/10.1016/j.epsl.2009.08.036

1002 Mirouse, R., Barrère, P., 1993. Carte géologique de la France a 1/50000. Vielle-Aure
1003 (1083). BRGM. Service Géologique National.

1004 Mochales, T., 2011. Chronostratigraphy, Vertical Axis Rotations and Ams in the
1005 Boltaña Anticline (Southern Pyrenees): Kinematic Implications. (PhD)
1006 Universidad de Zaragoza, Zaragoza.

1007 Mochales, T., Pueyo, E.L., Casas, A.M., Barnolas, A., 2016. Restoring paleomagnetic
1008 data in complex superposed folding settings: The Boltaña anticline (Southern
1009 Pyrenees). Tectonophysics 671, 281–298.
1010 https://doi.org/10.1016/j.tecto.2016.01.008

1011 Muñoz, J.A., 1992. Evolution of a continental collision belt: ECORS-Pyrenees crustal
1012 balanced cross-section. In: McClay, K.R. (Ed.), Thrust Tectonics. Springer
1013 Netherlands, Dordrecht, 235–246. https://doi.org/10.1007/978-94-011-3066-0_21

1014 Muñoz, J.A., Martinez, A., Verges, J., 1986. Thrust sequences in the eastern Spanish
1015 Pyrenees. Journal of Structural Geology 8, 399–405.
1016 https://doi.org/https://doi.org/10.1016/0191-8141(86)90058-1

1017 Muñoz, J.A., Beamud, E., Fernández, O., Arbués, P., Dinarès-Turell, J., Poblet, J.,
1018 2013. The Ainsa Fold and thrust oblique zone of the central Pyrenees: Kinematics

1019 of a curved contractional system from paleomagnetic and structural data. Tectonics
1020 32, 1142–1175. https://doi.org/10.1002/tect.20070

1021 Oliva-Urcia, B., Larrasoaña, J.C., Pueyo, E.L., Gil, a., Mata, P., Parés, J.M., Schleicher,
1022 a. M., Pueyo, O., 2009. Disentangling magnetic subfabrics and their link to
1023 deformation processes in cleaved sedimentary rocks from the Internal Sierras (west
1024 central Pyrenees, Spain). Journal of Structural Geology 31, 163–176.
1025 https://doi.org/10.1016/j.jsg.2008.11.002

1026 Oliva-Urcia, B., Rahl, J.M., Schleicher, A.M., Parés, J.M., 2010. Correlation between
1027 the anisotropy of the magnetic susceptibility, strain and X-ray Texture Goniometry
1028 in phyllites from Crete, Greece. Tectonophysics 486, 120–131.

1029 Oliva-Urcia, B., Casas, A.M., Soto, R., Villalaín, J.J., Kodama, K., 2011. A
1030 transtensional basin model for the Organyà basin (central southern Pyrenees) based
1031 on magnetic fabric and brittle structures. Geophysical Journal International 184,
1032 111–130. https://doi.org/10.1111/j.1365-246X.2010.04865.x

1033 Oliva-Urcia, B., Casas, A. M., Ramón, M.J., Leiss, B., Mariani, E., Román-Berdiel, T.,
1034 2012a. On the reliability of AMS in ilmenite-type granites: An insight from the
1035 Marimanha pluton, central Pyrenees. Geophysical Journal International 189, 187–
1036 203. https://doi.org/10.1111/j.1365-246X.2011.05355.x

1037 Oliva-Urcia, B., Pueyo, E.L., Larrasoaña, J.C., Casas, A.M., Román-Berdiel, T., van der
1038 Voo, R., Scholger, R., 2012b. New and revisited paleomagnetic data from

1039 Permian-Triassic red beds: Two kinematic domains in the west-central Pyrenees.
1040 Tectonophysics 522–523, 158–175. https://doi.org/10.1016/j.tecto.2011.11.023

1041 Ono, T., Hosomi, Y., Arai, H., Takagi, H., 2010. Comparison of petrofabrics with
1042 composite magnetic fabrics of S-C mylonite in paramagnetic granite. Journal of
1043 Structural Geology 32, 2–14. https://doi.org/10.1016/j.jsg.2009.04.009

1044 Parés, J.M., Van Der Pluijm, B. A., 2002. Evaluating magnetic lineations (AMS) in
1045 deformed rocks. Tectonophysics 350, 283–298. https://doi.org/10.1016/S0040-
1046 1951(02)00119-1

1047 Parés, J.M., van der Pluijm, B. A., 2004. Correlating magnetic fabrics with finite strain:
1048 Comparing results from mudrocks in the Variscan and Appalachian Orogens.
1049 Geologica Acta 2, 213–220.

1050 Parish, M., 1984. A structural interpretation of a section of the Gavarnie nappe and its
1051 implications for Pyrenean geology. Journal of Structural Geology 6, 247–255.
1052 https://doi.org/10.1016/0191-8141(84)90049-X

1053 Pocoví Juan, A., Pueyo Anchuela, Pueyo, E.L., Casas-Sainz, A.M., Román Berdiel,
1054 M.T., Gil Imaz, A., Ramajo Cordero, J., Mochales, T., García Lasanta, C.,
1055 Izquierdo-Llavall, E., Parés, J.M., Sánchez, E., Soto Marín, R., Oliván, C.,
1056 Rodríguez Pintó, A., Oliva-Urcia, B., Villalaín, J.J., 2014. Magnetic fabrics in the
1057 Western Central-Pyrenees: An overview. Tectonophysics 629, 303–318.
1058 https://doi.org/10.1016/j.tecto.2014.03.027

1059 Potter, D.K., 2004. A comparison of anisotropy of magnetic remanence methods – a
1060 user's guide for application to paleomagnetism and magnetic fabric studies. In:
1061 Martín-Hernández, F., Lünenburg, C.M., Aubourg, C., Jackson, M. (Eds.),
1062 Magnetic Fabrics. Geological Society of London Special Publication, vol. 238, pp.
1063 21–35.

1064 Pueyo-Anchuela, Ó., Gil Imaz, A., Pocoví Juan, A., 2012. Factors affecting the record
1065 of strain fabrics at the anisotropy of magnetic susceptibility: West-Central South-
1066 Pyrenean cleavage domain (Southern Pyrenees; NE Spain). Tectonophysics 554–
1067 557, 1–17. https://doi.org/10.1016/j.tecto.2012.05.028

1068 Rahl, J.M., Haines, S.H., van der Pluijm, B.A., 2011. Links between orogenic wedge
1069 deformation and erosional exhumation: Evidence from illite age analysis of fault
1070 rock and detrital thermochronology of syn-tectonic conglomerates in the Spanish
1071 Pyrenees. Earth and Planetary Science Letters 307, 180–190.

1072 Ramsay, J.G., Graham, R.H., 1970. Strain variation in shear belts. Canadian Journal of
1073 Earth Sciences 7, 786–813. https://doi.org/10.1139/e70-078

1074 Rathore, J.S., Courrioux, G., Choukroune, P., 1983. Study of ductile shear zones
1075 (Galicia, Spain) using texture goniometry and magnetic fabric methods.
1076 Tectonophysics, 98(1-2), pp.87-109. https://doi.org/10.1016/0040-1951(83)90212-
1077 3

ACCEPTED MANUSCRIPT

1078 Ritcher, C., Van der Plujim, B.A., 1994. Separation of paramagnetic and ferrimagnetic
1079 susceptibilities using low temperature magnetic susceptibilities and comparison
1080 with high field methods. Phys. Earth Planet. Inter. 82, 113–123.

1081 Rochette, P., Jackson, M., Aubourg, C., 1992. Rock Magnetism and the Interpretation
1082 of Magnetic Susceptibility of. 209–226.

1083 Román-Berdiel, T., Casas, A.M., Oliva-Urcia, B., Pueyo, E.L., Rillo, C., 2004. The
1084 main Variscan deformation event in the Pyrenees: New data from the structural
1085 study of the Bielsa granite. Journal of Structural Geology 26, 659–677.
1086 https://doi.org/10.1016/j.jsg.2003.09.001

1087 Rosenbaum, G., Lister, G.S., Duboz, C., 2002. Relative motions of Africa, Iberia and
1088 Europe during Alpine orogeny. Tectonophysics 359, 117–129.
1089 https://doi.org/10.1016/S0040-1951(02)00442-0

1090 Ruf, A.S., Naruk, J., Butler, F., Calderone, G.J., 1988. Strain and magnetic fabric in the
1091 Santa Catalina and Pinaleno Mountains metamorphic core complex mylonite
1092 zones, Arizona. Tectonics 7, 235–248.

1093 Schellart, W.P., 2002. Alpine deformation at the western termination of the axial zone,
1094 Southern Pyrenees. Journal of the Virtual Explorer 8.
1095 https://doi.org/10.3809/jvirtex.2002.00055

1096 Schultz-Krutisch, T., Heller, F., 1985. Measurement of magnetic susceptibility
1097 anisotropy in Buntsandstein deposits from southern Germany. J. Geophys. 56, 51–
1098 58.

ACCEPTED MANUSCRIPT

1099 Séguret, M., 1972. Etude tectonique des nappes de séries décollées de la partie centrale
1100 du versant sud des Pyrénées. Caractère synsédimentaire, rôle de la compression et
1101 de la gravité. Thèse Doct. Publ. USTELA, Série Géologique, Montpellier, 155 pp.

1102 Sibson, R.H., 1977. Fault rocks and fault mechanisms. Journal of the Geological
1103 Society 133, 191–213. https://doi.org/10.1144/gsjgs.133.3.0191

1104 Sidman, D., Ferré, E.C., Teyssier, C., Jackson, M., 2005. Magnetic fabric and
1105 microstructure of a mylonite: example from the Bitterroot shear zone, western
1106 Montana. Geological Society, London, Special Publications 245, 143–163.
1107 https://doi.org/10.1144/GSL.SP.2005.245.01.07

1108 Smeraglia, L., Aldega, L., Billi, A., Carminati, E., Doglioni, C., 2016. Phyllosilicate
1109 injection along extensional carbonate-hosted faults and implications for co-seismic
1110 slip propagation: Case studies from the central Apennines, Italy. Journal of
1111 Structural Geology 93, 29–50. https://doi.org/10.1016/j.jsg.2016.10.003

1112 Solum, J.G., van der Pluijm, B. a., 2009. Quantification of fabrics in clay gouge from
1113 the Carboneras fault, Spain and implications for fault behavior. Tectonophysics
1114 475, 554–562. https://doi.org/10.1016/j.tecto.2009.07.006

1115 Soula, J.C., Debat, P., Deramond, J., Pouget, P., 1986. The Geological Evolution of the
1116 Pyrenees A dynamic model of the structural evolution of the Hercynian Pyrenees.
1117 Tectonophysics 129, 29–51. https://doi.org/10.1016/0040-1951(86)90244-1

1118 Stephenson, A., Sadikun, S., Potter, D.K., 1986. A theoretical and experimental
1119 comparison of the anisotropies of magnetic-susceptibility and remanence in rocks

1120 and minerals. Geophysical J. Royal Astronomical Soc. 84, 185–200.
1121 https://doi.org/10.1111/j.1365-246X.1986.tb04351.x

1122 Tarling, D.H., Hrouda, F., 1993. The Magnetic Anisotropy of Rocks. Chapman & Hall,
1123 London, pp. 1–64.

1124 Teixell, A., 1998. Crustal structure and orogenic material budget in the west central
1125 Pyrenees. Tectonics 17, 395–406. https://doi.org/10.1029/98TC00561

1126 Tikoff, B., Davis, M.R., Teyssier, C., de St. Blanquat, M., Habert, G., Morgan, S., 2005.
1127 Fabric studies within the Cascade Lake shear zone, Sierra Nevada, California.
1128 Tectonophysics 400, 209–226. https://doi.org/10.1016/j.tecto.2005.03.003

1129 Tomezzoli, R.N., MacDonald, W.D., Tickyj, H., 2003. Composite magnetic fabrics and
1130 S-C structure in granitic gneiss of Cerro de los Viejos, La Pampa province,
1131 Argentina. Journal of Structural Geology 25, 159–169.
1132 https://doi.org/10.1016/S0191-8141(02)00030-5

1133 Verberne, B.A., Niemeijer, A.R., De Bresser, J.H.P., Spiers, C.J., 2015. Mechanical
1134 behavior and microstructure of simulated calcite fault gouge sheared at 20–600°C:
1135 Implications for natural faults in limestones. Journal of Geophysical Research:
1136 Solid Earth 120, 8169–8196. https://doi.org/10.1002/2015JB012292

1137 Williams, G.D., Fischer, M.W., 1984. A balanced section across the Pyrenean Orogenic
1138 Belt. Tectonics 3, 773–780. https://doi.org/10.1029/TC003i007p00773

ACCEPTED MANUSCRIPT

1139 Zhang, L., He, C., 2016. Frictional properties of phyllosilicate-rich mylonite and
1140 conditions for the brittle-ductile transition. Journal of Geophysical Research: Solid
1141 Earth 121, 3017–3047. https://doi.org/10.1002/2015JB012489

1142 Zhou, Y., Zhou, P., Min, S., Bin, X., Jiang, J., 2002. Magnetic fabric study across the
1143 Ailao Shan – Red River shear zone. Geology 346, 137–150.
1144 https://doi.org/10.1016/S0040-1951(01)00269-4

1145 **Table captions**

1146 Table 1. X-ray diffraction mineralogical assemblages of fault rocks.

1147 DTP, Distance to the thrust plane; SP, Silurian Phyllites; DPL, Devonian phyllites and
1148 limestones; Phy, phyllosilicates; Qtz, Quartz; Cal, calcite; Dol, dolomite; Kfs, K-feldspar;
1149 Plg, plagioclase; Pyr, pyrite; Msc, Moscovite; Prg, Paragonite; Chl, chlorite; Tal, talc; I-S,
1150 mixed layers illite-smectite; Kln, kaolinite;

1151 Table 2. Summary of magnetic scalar data and structural patterns.

1152 Km, average value of magnetic susceptibility; Pj, corrected degree of anisotropy; L,
1153 lineation parameter; F, foliation parameter; T, shape parameter; e, standard deviation;
1154 D, declination; I, Inclination.

1155 Table 3. Summary of magnetic scalar data for LT-AMS and AIRM measurements.

1156 Km, average value of magnetic susceptibility; Pj, corrected degree of anisotropy; L,
1157 lineation parameter; F, foliation parameter; T, shape parameter. ST., standard
1158 deviation D, declination; I, Inclination; LT/RT, ratio of magnetic susceptibility at low

ACCEPTED MANUSCRIPT

1159 temperature and at room temperature; RMS error, the tensor fit. Declination,
1160 inclination and confidence angles cannot be obtained for AIRM measurements
1161 because of the low number of specimens measured by site.

1162

1163 **Figure captions**

1164 Fig. 1. a) Geological sketch map of the Pyrenees (modified from Teixell, 1996, and
1165 Izquierdo-Llavall *et al.*, 2015) with the location of the study area. AZ, Axial Zone; SPCU,
1166 South Pyrenean Central Unit; SPZ, South Pyrenean Zone; IS, Internal Sierras; NPF,
1167 North Pyrenean Fault; GT, Gavarnie Thrust. b) Schematic geological cross-section
1168 across the study area, indicated by a red star (modified from Martínez-Peña and Casas-
1169 Sainz, 2003, and Izquierdo-Llavall *et al.*, 2015). c) Geological map of the study area and
1170 related outcrops (red box) of the Gavarnie Thrust.

1171 Fig. 2. Interpreted panoramic view of the Gavarnie thrust (GT) around the studied
1172 outcrops, Barrosa Valley. b) Younger Devonian formations are progressively involved
1173 within the shear zone towards the South. c) Alpine recumbent anticline in the
1174 hangingwall of the GT, whose overturned limb is involved within the shear zone. d)
1175 Silurian phyllites overthrusting Mesozoic units.

1176 Fig. 3. Schematic diagram showing the structural patterns observed in Profile B with
1177 position of AMS sites and their distance from the basal thrust. a-j) Outcrop pictures
1178 and photomicrographs of selected sites for the AMS study. S-C structures are dominant
1179 in the lowermost 11 m, both in field (a, c, e) and microstructural observations (b, d),

1180 whereas Variscan foliations and Alpine brittle shear bands (f-j) dominate in the upper
1181 part of the section. See text for more details. Photomicrographs of thin sections were
1182 done in XZ and YZ sections with parallel polarizers, x2.5 lens. Qtz, quartz; Phy,
1183 phyllosilicates; Pyr, pyrite. P: P-Riedel fractures.

1184 Fig. 4. Schematic diagram showing the structural patterns observed in Profile A with
1185 position of AMS sites and their distance from the basal thrust. a-j) Outcrop pictures
1186 and photomicrographs of sites selected for the AMS study. S-C structures in Silurian
1187 phyllites (a-d) are dominant in the lowermost 5 m of the profile. Upwards, C parallel
1188 foliations (e), S-C-C' structures (g) and poorly developed S-C structures (i) are
1189 observed. In thin section, progressively decreasing development of foliation was
1190 observed (f, h, j). See text for more details. All thin section photographs were done
1191 with parallel polarizers, x2.5 lens. Qtz, quartz; Phy, phyllosilicates; Pyr, pyrite; Cal,
1192 calcite.

1193 Fig. 5. Stereoplots of the structural data. a) foliation, S planes. b) shear, C planes. c)
1194 stretching lineations, and transport direction inferred from S-C structures. Lower-
1195 hemisphere, equal-area projections. Kamb contour, contour interval 2%.

1196 Fig. 6. a-c) Temperature-dependent magnetic susceptibility (K-T) curves in Silurian
1197 phyllites (a) and Devonian limestones and phyllites (b, c); d) IRM acquisition curves for
1198 three samples; e) Stepwise thermal demagnetization of the composite IRM.

1199 Fig. 7. EDS-SEM chemical analyses. Colours are indicative of the relative dominance of
1200 a certain element over the other selected elements. a) Silurian phyllonite; b) mylonitic

Devonian limestone; c) fracture pattern in pyrite and its replacement by iron oxides; Qtz, quartz; Chl, chlorite; Ms, muscovite-phengite; Pyr, Pyrite; Fe ox., iron oxides; Cal, calcite. C, shear planes; S, foliation planes.

Fig. 8. Evolution of the bulk susceptibility (a) and Pj (b) by sites along the the profile B, and diagrams showing the corrected degree of anisotropy vs. bulk anisotropy by samples (c). Black and grey bars in a) and b) indicate magnetic lineations parallel or perpendicular to transport direction, respectively. d) Pj-T diagram showing the evolution of the magnetic fabric along Profile B. Ba17-6 and Ba17-10 are not considered in b), c) and d) because of their anomalous Pj values related to very low susceptibilities.

Fig. 9. a) Location of the RT-AMS sites along the basal profile and their equal-area, lower-hemisphere projections, with confidence ellipses. The position of the two vertical profiles (Fig. 10) is also shown. B) Silurian phyllites overthrusting Devonian limestones, showing different rheologies and mechanism deformation. C) Mylonitic foliations developed in Devonian limestones. D) S-C-C' structures developed in phyllosilicates in the Silurian phyllites. Thin-section photographs were done in XZ and YZ sections with parallel polarizers, x2.5 lens.

Fig. 10. Equal-area, lower-hemisphere projections of the magnetic ellipsoids for all sites in vertical profiles B and A. Meters indicate the height from the décollement for each sample.

ACCEPTED MANUSCRIPT

ACCEPTED MANUSCRIPT

Fig. 11. a) Comparative results of the different methods used for subfabric separation: RT-AMS (white symbols), LT-AMS (grey symbols) and AIRM (black symbols), and their confidence ellipses (only for RT- and LT-AMS). b) Ratio between the magnetic susceptibility at low and room temperature (LT/RT). Lower-hemisphere, equal-area projections.

Fig. 12. a) Tectonic sketch of the southern zone of the Pyrenees, showing the main structures, the inferred local transport direction (blue arrows) and vertical axis rotation identified in Muñoz et al. (2013) in the Mesozoic cover, and the transport direction obtained in this work for the Gavarnie Unit (red arrows). b) Geological cross section of the southern zone of the Pyrenees. Red color: basement detachment levels. Blue color: the Mesozoic cover detachment levels. V.A.R.: Vertical axis rotation; th.: Thrust; ant.: anticline.

Table 1. X-ray diffraction mineralogical assemblages of fault rocks.

				Whole rock composition (wt%)							<2µm grain size fraction (wt%)					
	Site	DTP	Lithology	Phy	Qtz	Cal	Dol	Kfs	Plg	Pyr	Msc	Par	Chl	Tal	I-S	Kln
PROFILE B	Cp7	0	SP	71	20	1	-	6	-	2	21	-	20	45	7	7
	Cp8	6	SP	73	18	-	-	8	-	1	41	-	59	-	-	-
	Ba17(4)	8	SP	79	15	-	-	6	-	-	-	-	-	-	-	-
	Ba17(12)	15	SP	63	32	-	1	3	-	1	38	26	36	-	-	-
	Ba17(9)	23	SP	69	24	-	-	7	-	-	-	-	-	-	-	-
	Ba17(11)	37	SP	51	32	-	1	15	-	1	-	-	-	-	-	-
PROFILE A	Cp1	0	SP	71	17	-	-	6	-	6	49	11	40	-	-	-
	Cp2	3	SP	77	16	-	-	7	-	-	59	11	30	-	-	-
	ba10	5	SP	55	18	16	1	6	-	4	51	3	46	-	-	-
	ba11(1)	7	DPL	50	10	36	1	-	1	2	63	-	37	-	-	-
	ba11(3)	10	DPL	25	5	66	1	2	-	1	41	-	59	-	-	-
	Cp6	17	DPL	50	12	25	2	5	-	6	-	-	-	-	-	-

DTP, Distance to the thrust plane; SP, Silurian Phyllites; DPL, Devonian phyllites and limestones; Phy, phyllosilicates; Qtz, Quartz; Cal, calcite; Dol, dolomite; Kfs, K-feldspar; Plg, plagioclase; Pyr, pyrite; Msc, Moscovite; Prg, Paragonite; Chl, chlorite; Tal, talc; I-S, mixed layers illite-smectite; Kln, kaolinite;

ACCEPTED MANUSCRIPT

Table 2. Summary of magnetic scalar data and structural patterns.

	Site	N	Km (E^{-6} SI)	e	Pj	e	L	e	F	e	T	e	Kmax D/I	Conf ang.	Kmin D/I	Conf ang.	Pole S plane	Pole C plane	Lineation
Horizontal profile	BA2	15	102	38	1.113	0.011	1.012	0.006	1.090	0.011	0.762	0.127	40/23	32/11	182/62	13/05	197, 55	207, 64	004, 26
	BA4	13	47	26	1.174	0.061	1.041	0.035	1.120	0.038	0.543	0.280	22/20	20/10	200/70	15/08	203, 68	-	-
	BA7	18	158	65	1.159	0.048	1.029	0.013	1.117	0.039	0.578	0.180	352/27	20/12	175/62	13/08	171, 47	166, 71	350, 20
	BA8	14	30	10	1.251	0.055	1.067	0.017	1.165	0.047	0.388	0.168	180/10	15/06	66/68	11/07	177, 40	185, 64	157, 24
	BA12	14	114	40	1.061	0.017	1.029	0.012	1.030	0.016	-0.009	0.344	332/36	10/07	106/44	13/06	160, 41	-	-
	BA14	27	171	46	1.116	0.040	1.026	0.014	1.082	0.031	0.503	0.220	08/24	15/11	149/60	22/11	165, 45	176, 74	019, 16
	BA22	14	131	34	1.098	0.021	1.045	0.013	1.049	0.022	0.002	0.342	19/22	14/10	182/67	18/12	177, 51	178, 68	018, 26
	BA20	27	105	32	1.119	0.024	1.027	0.007	1.084	0.022	0.486	0.158	199/03	10/06	61/87	07/06	198, 56	195, 72	025, 33
Profile A	CP1	8	167	18	1.178	0.038	1.031	0.009	1.132	0.033	0.599	0.147	350/29	25/07	169/61	19/07	200, 52	220, 69	340, 20
	CP2	11	213	56	1.085	0.022	1.029	0.012	1.051	0.023	0.224	0.387	176/04	14/13	303/84	28/12	157, 39	145, 54	002, 30
	BA10	22	174	40	1.168	0.04	1.030	0.016	1.124	0.035	0.589	0.207	06/30	09/09	144/52	09/07	150, 54	124, 62	008, 13
	BA11-1	45	112	38	1.109	0.029	1.030	0.013	1.072	0.032	0.347	0.374	306/23	16/05	133/67	10/05	109, 61	Vertical	000, 12
	BA11-2	8	66	11	1.223	0.029	1.068	0.030	1.138	0.040	0.317	0.321	30/05	08/04	128/59	04/04	144, 35	-	011, 44
	BA11-3	15	67	27	1.152	0.033	1.061	0.032	1.083	0.022	0.167	0.342	199/10	15/10	82/69	20/11	080, 47	-	004, 08
	CP5	8	152	49	1.356	0.153	1.120	0.103	1.202	0.045	0.322	0.291	25/31	12/05	163/52	13/05	148, 39	Vertical	-
	BA11-4	13	122	50	1.216	0.123	1.126	0.080	1.072	0.055	-0.267	0.429	21/14	16/08	138/62	20/08	116, 68	151, 59	000, 20
	CP6	10	131	22	1.212	0.069	1.025	0.008	1.164	0.060	0.689	0.142	00/13	45/13	135/72	15/06	134, 62	115, 80	-
Profile B	CP7	13	169	37	1.170	0.039	1.023	0.008	1.131	0.034	0.672	0.137	06/17	11/09	146/69	11/08	185, 59	174, 65	352, 32
	BA17-1	11	61	24	1.246	0.043	1.030	0.007	1.190	0.036	0.704	0.075	355/00	08/04	100/89	09/04	170, 57	164, 76	356, 33
	CP8	7	158	29	1.115	0.017	1.027	0.011	1.081	0.020	0.479	0.241	31/33	15/06	142/28	14/11	162, 37	148, 64	-
	BA17-4	10	112	24	1.118	0.017	1.023	0.009	1.087	0.016	0.560	0.163	29/24	06/03	169/60	07/03	155, 45	163, 72	356, 44
	BA17-5	25	87	17	1.104	0.017	1.035	0.014	1.065	0.020	0.289	0.288	296/16	16/04	154/70	22/04	197, 57	182, 77	-
	BA17-6	13	68	9	1.761	0.845	1.121	0.088	1.367	0.054	0.559	0.227	50/00	13/02	142/68	05/02	145, 69	Vertical	-
	BA17-12	8	79	10	1.300	0.023	1.032	0.007	1.234	0.022	0.738	0.062	95/06	10/05	189/40	20/05	180, 54	-	-
	BA17-7	31	31	19	1.175	0.111	1.050	0.024	1.113	0.079	0.306	0.162	74/03	04/03	169/63	07/03	169, 60	-	018, 26
	BA17-9	12	55	15	1.212	0.031	1.083	0.012	1.118	0.019	0.166	0.061	63/01	06/02	156/69	04/02	155, 68	-	-
	BA17-10	11	11	9	1.518	0.655	1.117	0.074	1.625	0.544	0.487	0.230	14/29	15/01	138/46	01/01	150, 60	-	336, 30
	BA17-11	13	49	20	1.350	0.090	1.029	0.015	1.276	0.078	0.773	0.127	299/05	14/03	203/50	11/05	211, 43	225, 62	028, 46

Km, average value of magnetic susceptibility; Pj, corrected degree of anisotropy; L, lineation parameter; F, foliation parameter; T, shape parameter. e, standard deviation D, declination; I, Inclination;

ACCEPTED MANUSCRIPT

Table 3. Summary of magnetic scalar data for LT-AMS and AIRM measurements.

LT-AMS

Site	N	Km (E^{-6} SI)	St.	Pj	L	F	T	Kmax (D/I)	Conf. ang.	Kmin (D/I)	Conf. ang.	LT/RT
Ba7	7	474	245	1.192	1.031	1.143	0.602	012/24	26/15	174/65	18/13	3.02
Cp7	6	697	76	1.230	1.019	1.184	0.773	006/20	28/09	149/66	10/08	3.72
Ba17-1	7	158	40	1.233	1.024	1.183	0.748	349/02	13/04	088/79	12/4	2.61
Ba17-12	6	290	53	1.314	1.036	1.242	0.718	096/01	15/10	187/33	28/10	3.63
Ba17-7	7	61	45	1.122	1.038	1.077	0.281	075/04	03/02	175/70	09/02	2.92
Ba10	6	650	92	1.190	1.037	1.138	0.542	001/30	12/04	167/51	09/03	3.26
Ba11-2	5	142	26	1.289	1.073	1.191	0.424	210/11	12/03	097/63	11/04	2.20
Cp6	6	441	66	1.183	1.029	1.159	0.646	349/13	26/14	130/73	15/08	3.21

AIRM

Site	N	Km (E^{-6} SI)	St.	Pj	L	F	T	Kmax (D/I)	Conf ang	Kmin (D/I)	Conf ang	RMS error
Ba7	4	0.1383	0.0968	1.195	1.056	1.122	0.349	-	-	-	-	1.8%
Cp7	3	0.1045	0.0433	1.354	1.189	1.135	0.126	-	-	-	-	4.6%
Ba17-12	4	0.0368	0.0057	1.357	1.118	1.209	0.260	-	-	-	-	1.3%
Ba17-11	4	0.0272	0.0176	1.140	1.054	1.077	0.300	-	-	-	-	1.1%
Ba10	4	0.2812	0.3048	1.192	1.044	1.132	0.455	-	-	-	-	1.0%
Cp6	3	0.2013	0.0411	1.255	1.102	1.136	0.126	-	-	-	-	0.5%

Km, average value of magnetic susceptibility; Pj, corrected degree of anisotropy; L, lineation parameter; F, foliation parameter; T, shape parameter. ST., standard deviation D, declination; I, Inclination; LT/RT, ratio of magnetic susceptibility at low temperature and at room temperature; RMS error, average of the tensor fit. Declination, inclination and confidence angles can not be obtained for AIRM measurements because of the low number of specimens measured by site.

ACCEPTED MANUSCRIPT

ACCEPTED MANUSCRIPT

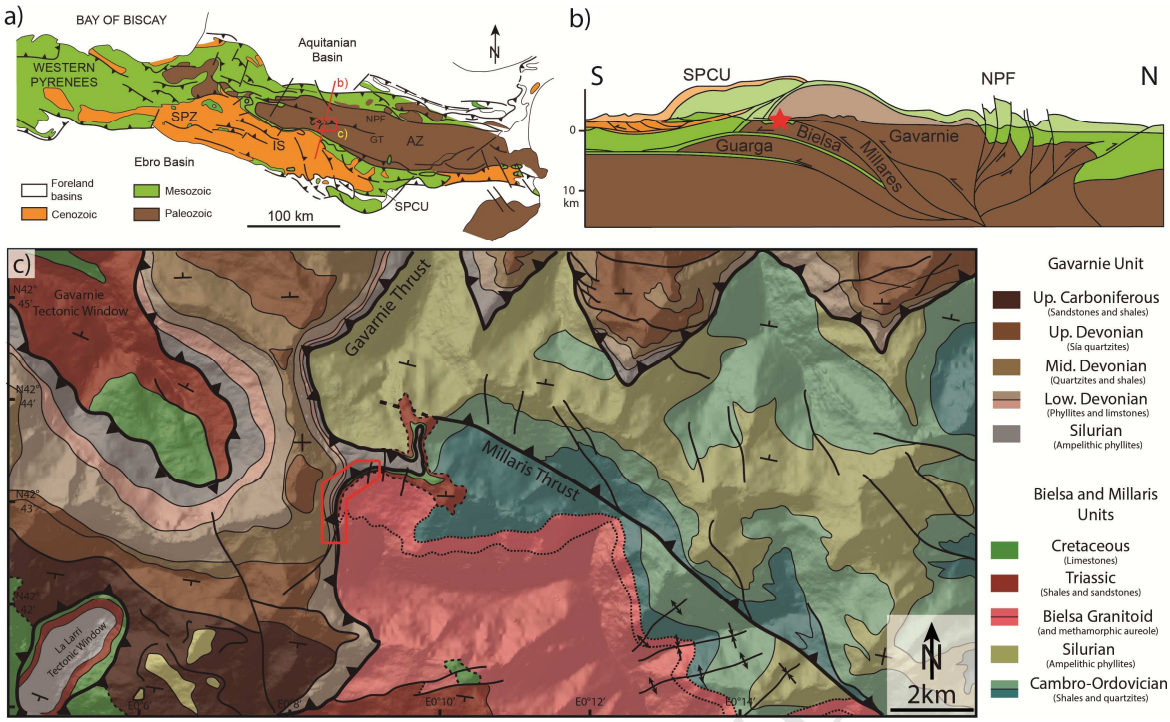

ACCEPTED MANUSCRIPT

ACCEPTED MANUSCRIPT

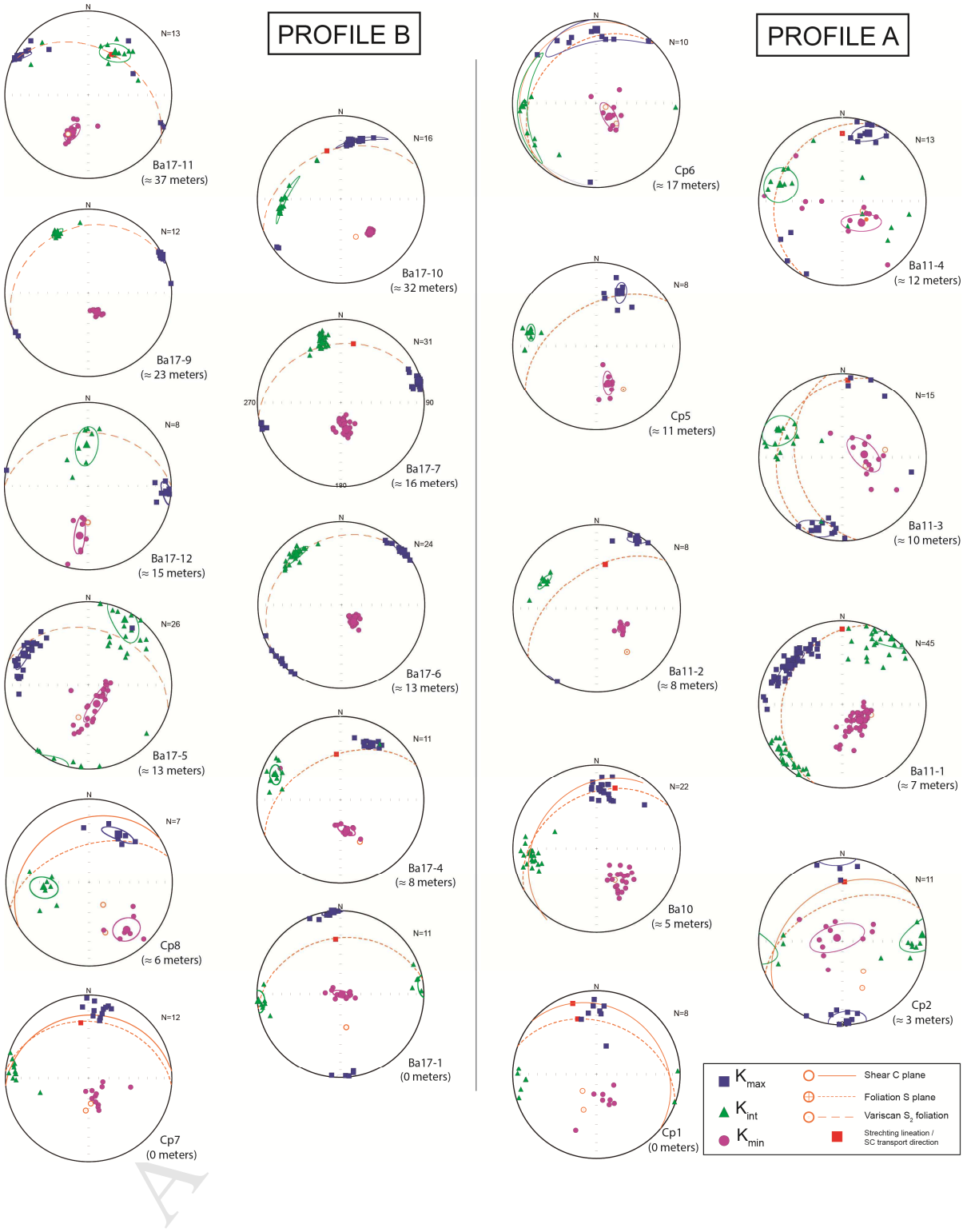

ACCEPTED MANUSCRIPT

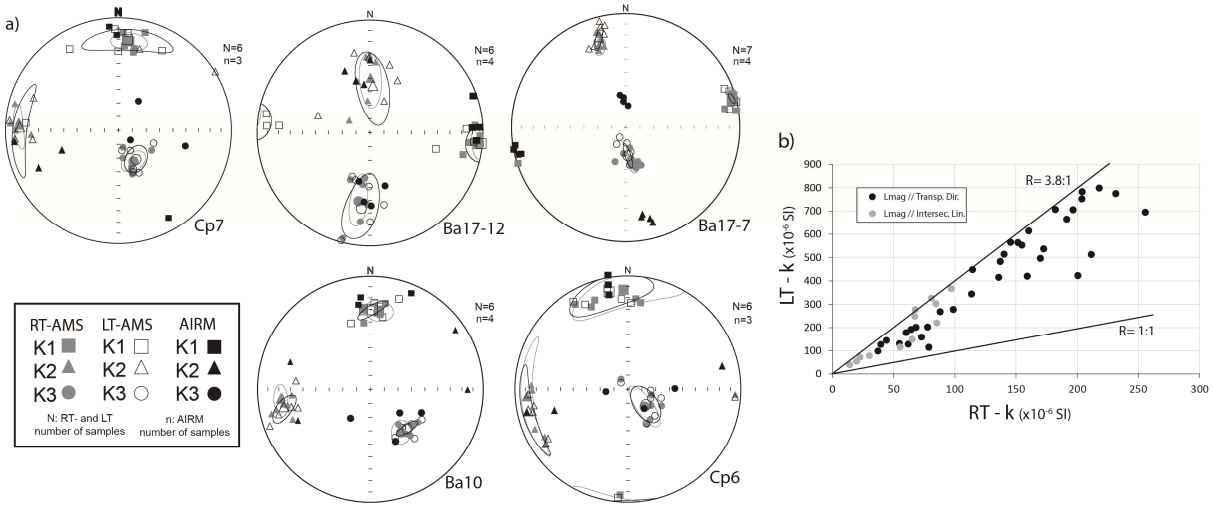

ACCEPTED MANUSCRIPT

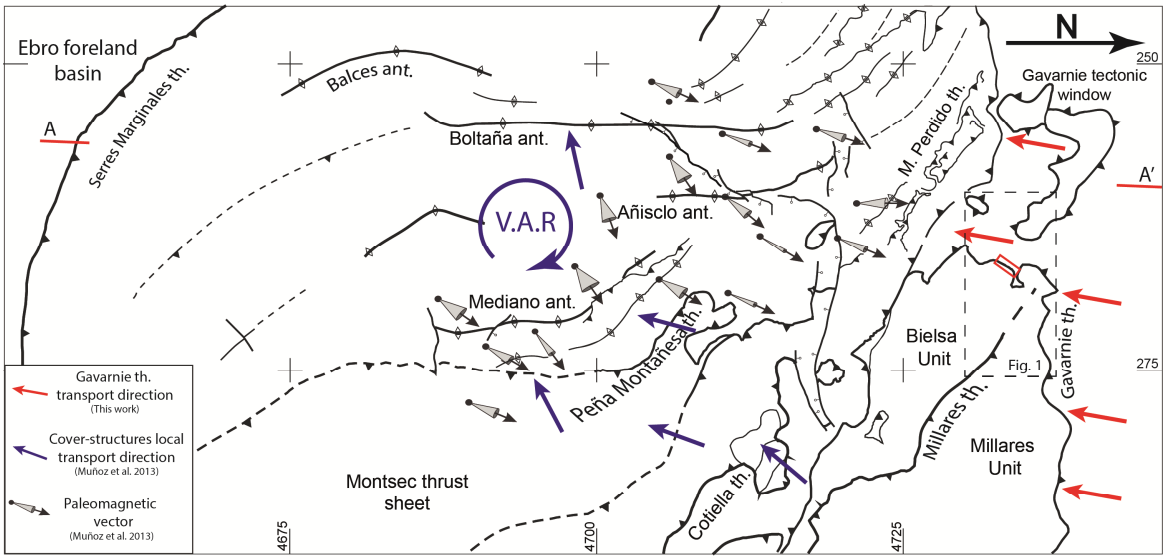

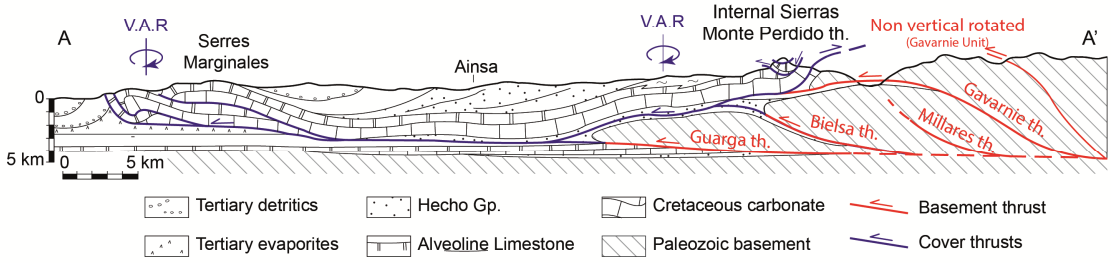

ACCEPTED MANUSCRIPT

ACCEPTED MANUSCRIPT

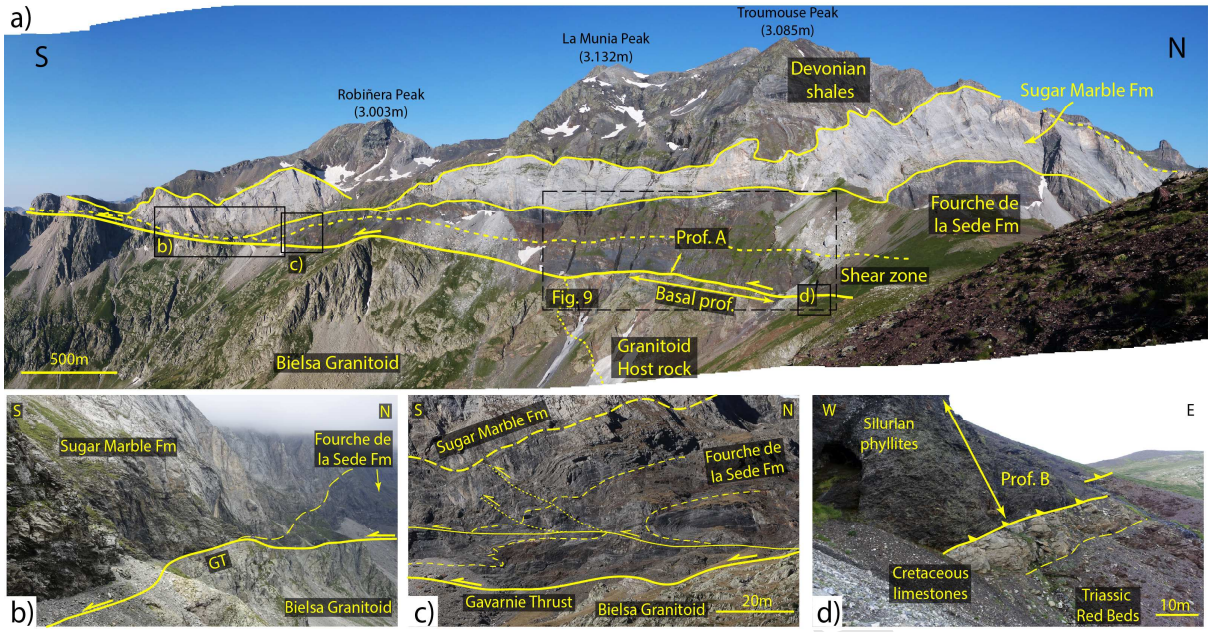

ACCEPTED MANUSCRIPT

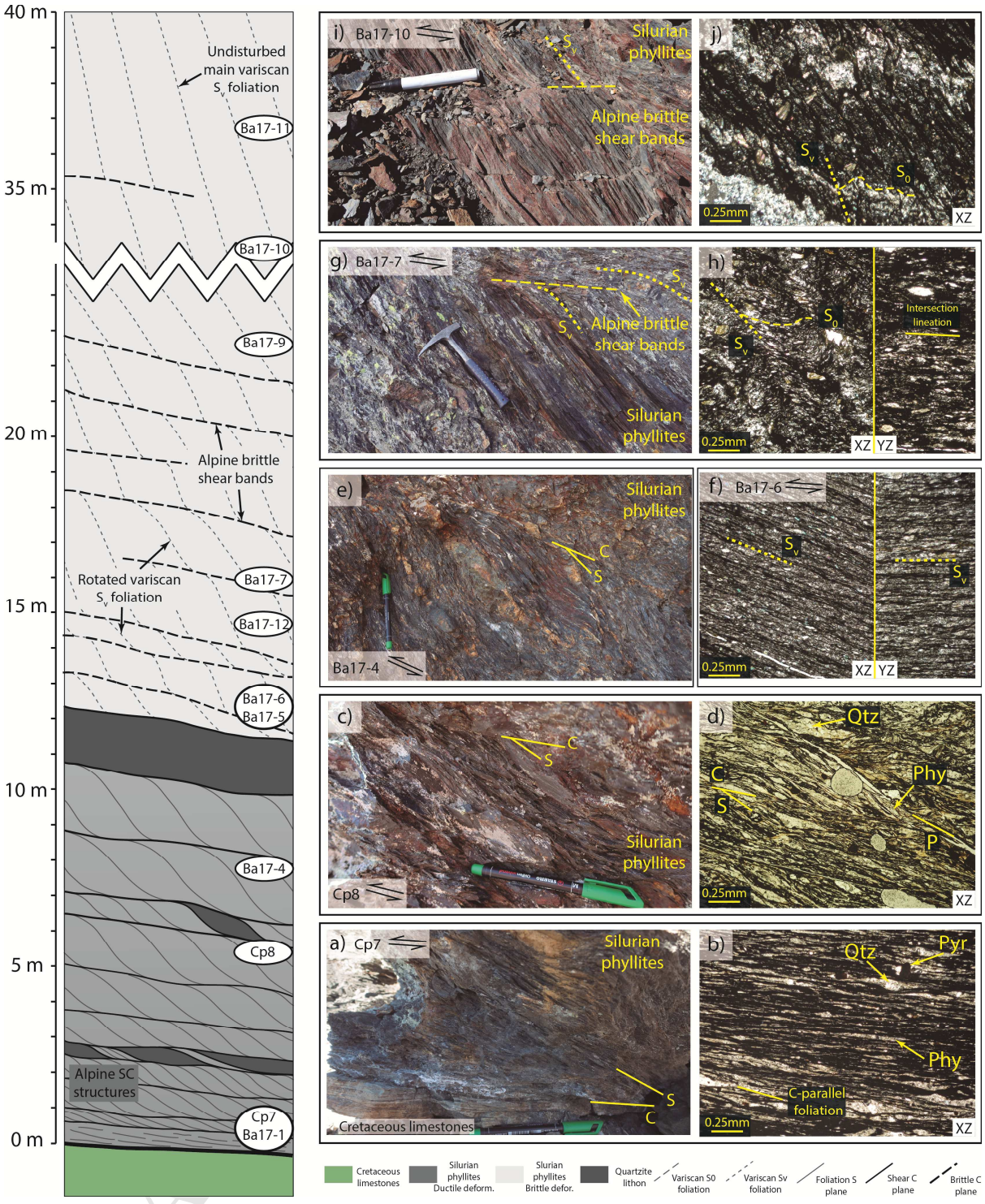
40 m
35 m
20 m
15 m
10 m
5 m
0 m
Undisturbed main variscan S$_v$ foliation
Ba17-11
Ba17-10
Ba17-9
Alpine brittle shear bands
Rotated variscan S$_v$ foliation
Ba17-7
Ba17-12
Ba17-6
Ba17-5
Ba17-4
Cp8
Alpine SC structures
Cp7
Ba17-1
i) Ba17-10
Silurian phyllites
Alpine brittle shear bands
j)
0.25mm
XZ
g) Ba17-7
Silurian phyllites
h)
Intersection lineation
XZ YZ
e)
Ba17-4
f) Ba17-6
c)
Cp8
d)
Qtz
Phy
P
a) Cp7
Cretaceous limestones
b)
Pyr
C-parallel foliation
Cretaceous limestones
Silurian phyllites Ductile deform.
Silurian phyllites Brittle defor.
Quartzite lithon
Variscan S0 foliation
Variscan Sv foliation
Foliation S plane
Shear C plane
Brittle C plane

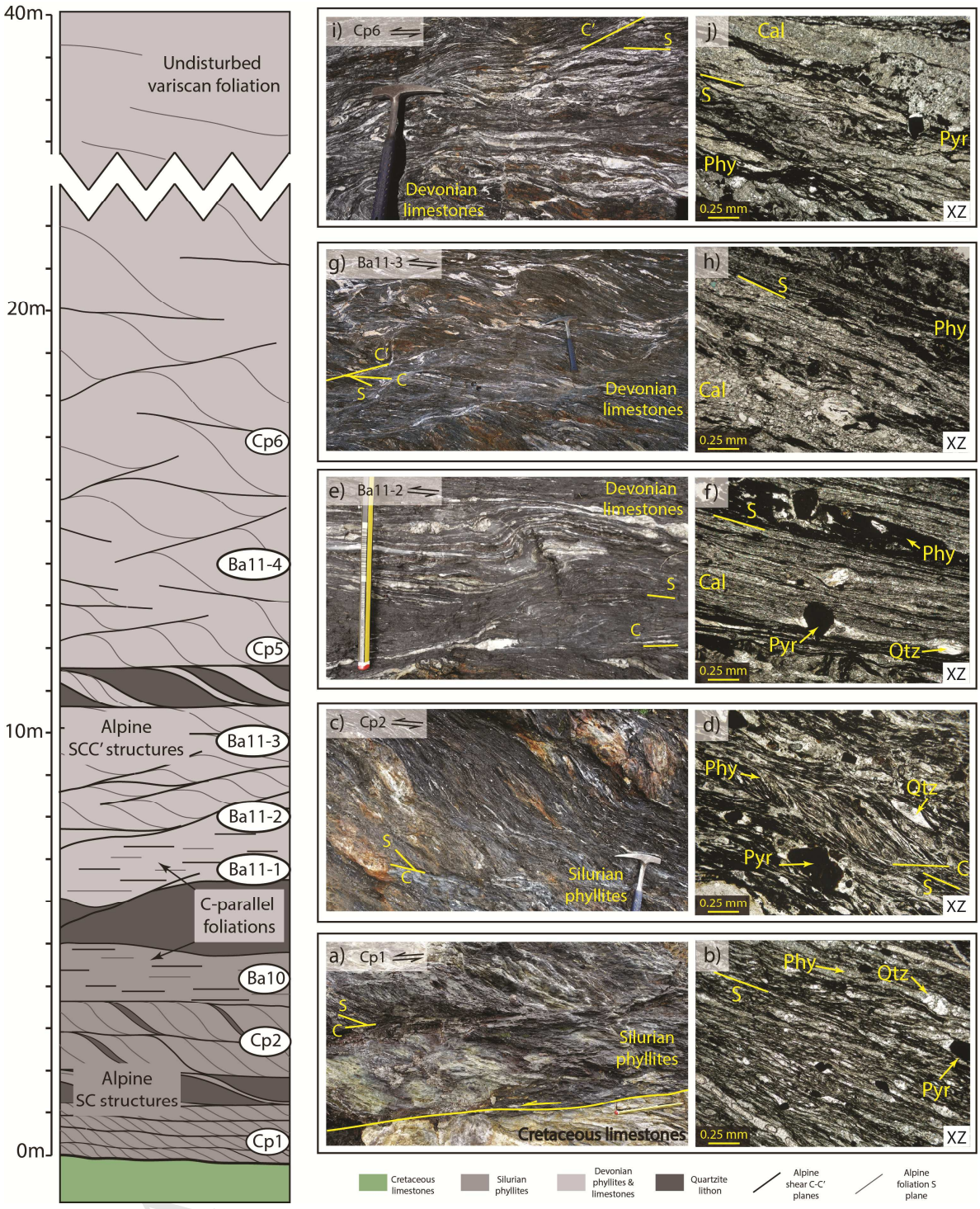
40m
20m
10m
0m
Undisturbed variscan foliation
Cp6
Ba11-4
Cp5
Alpine SCC' structures
Ba11-3
Ba11-2
Ba11-1
C-parallel foliations
Ba10
Cp2
Alpine SC structures
Cp1
i) Cp6
C'
S
Devonian limestones
j)
Cal
S
Pyr
Phy
0.25 mm
XZ
g) Ba11-3
C'
C
S
Devonian limestones
h)
S
Phy
Cal
0.25 mm
XZ
e) Ba11-2
Devonian limestones
S
C
f)
S
Phy
Cal
Pyr
Qtz
0.25 mm
XZ
c) Cp2
S
C
Silurian phyllites
d)
Phy
Qtz
Pyr
C
S
0.25 mm
XZ
a) Cp1
S
C
Silurian phyllites
Cretaceous limestones
b)
Phy
Qtz
S
Pyr
0.25 mm
XZ
Cretaceous limestones
Silurian phyllites
Devonian phyllites & limestones
Quartzite lithon
Alpine shear C-C' planes
Alpine foliation S plane

ACCEPTED MANUSCRIPT

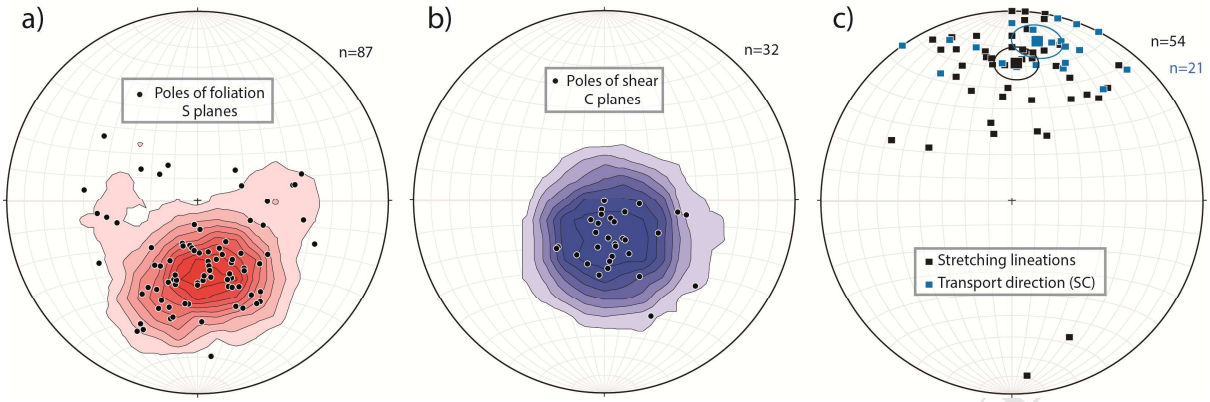

ACCEPTED MANUSCRIPT

ACCEPTED MANUSCRIPT

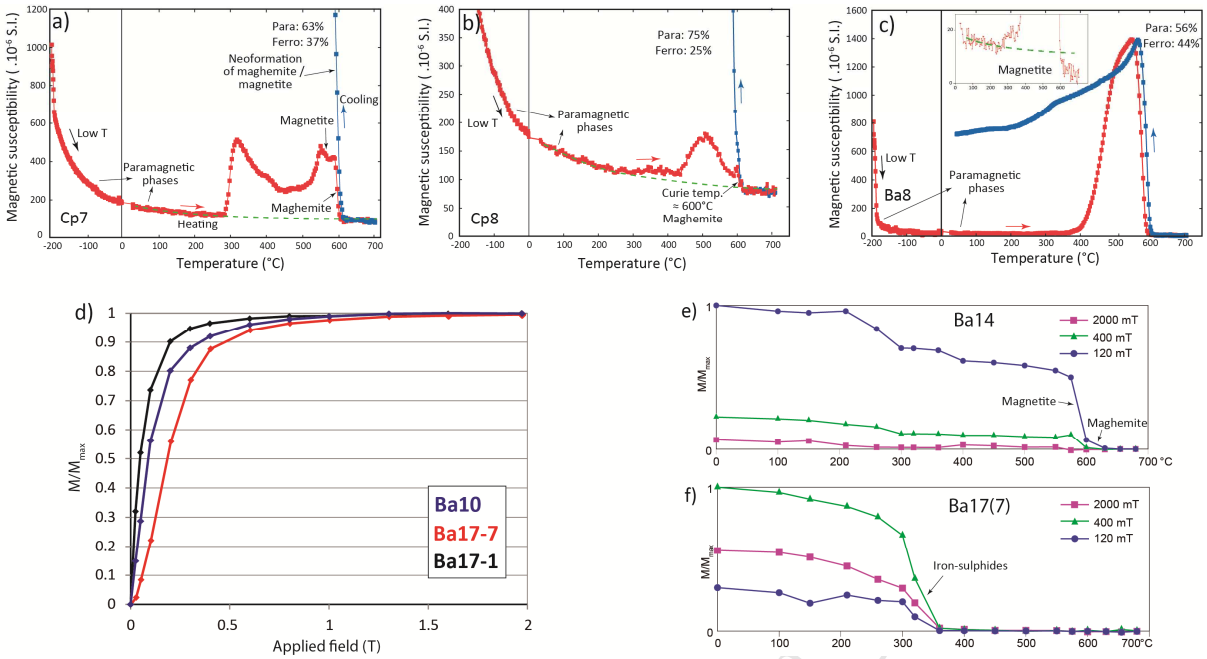

ACCEPTED MANUSCRIPT

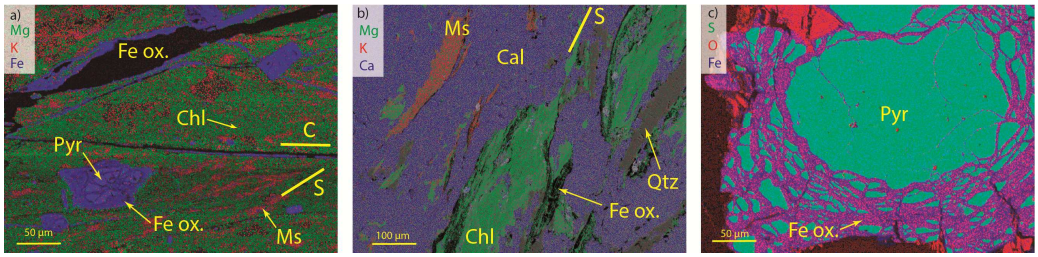

ACCEPTED MANUSCRIPT

ACCEPTED MANUSCRIPT

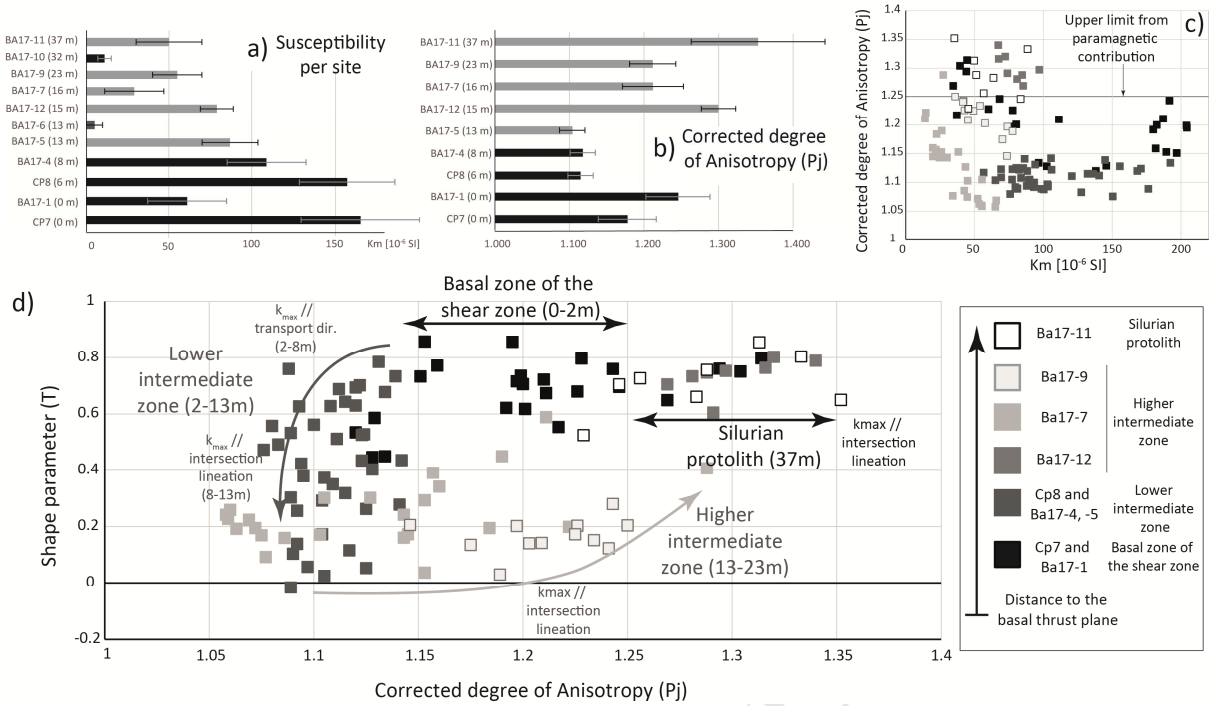

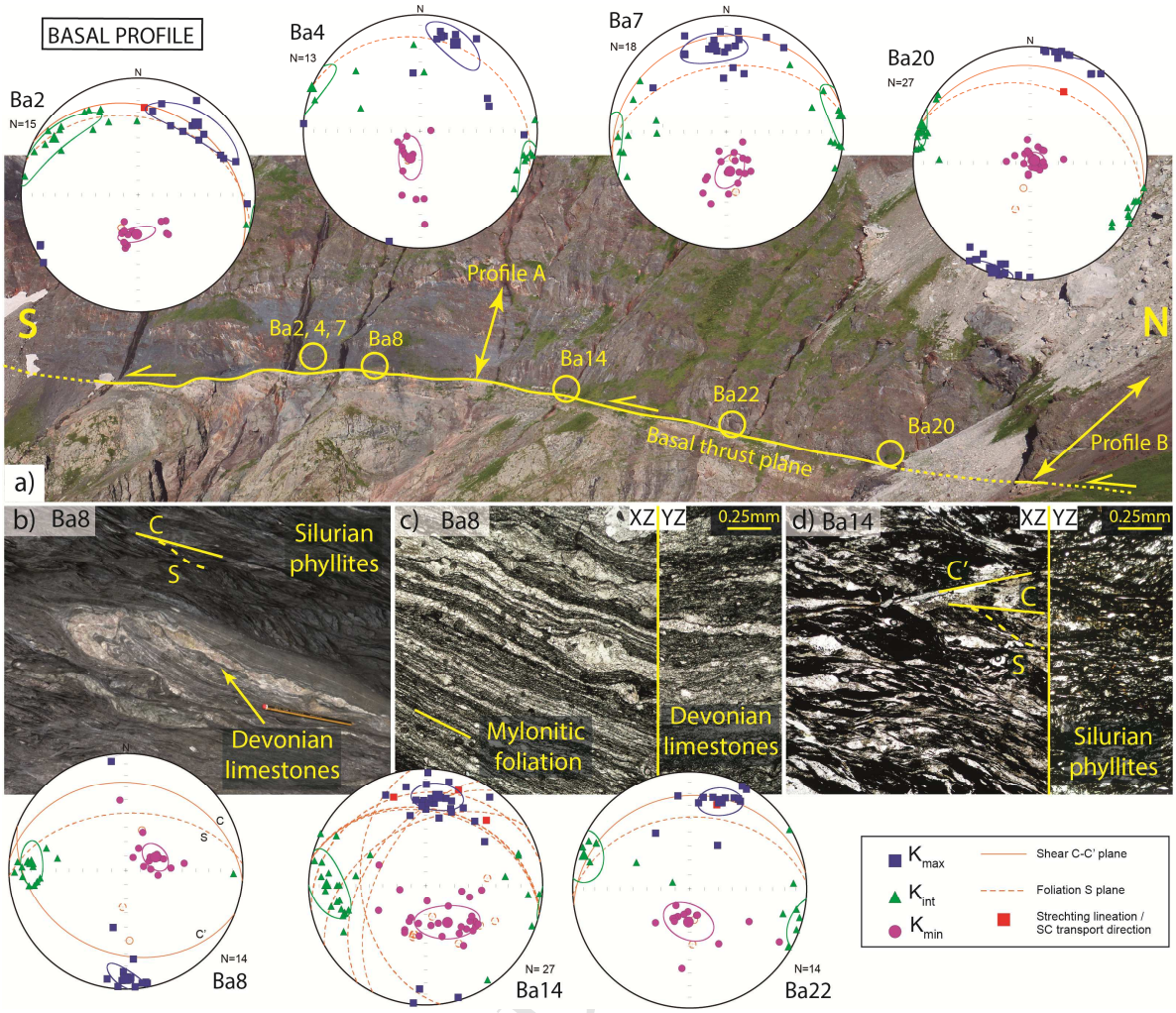
BASAL PROFILE
Ba2
N=15
Ba4
N=13
Ba7
N=18
Ba20
N=27
S
N
Profile A
Ba2, 4, 7
Ba8
Ba14
Ba22
Ba20
Basal thrust plane
Profile B
a)
b) Ba8
C
S
Silurian phyllites
Devonian limestones
c) Ba8
XZ
YZ
0.25mm
Mylonitic foliation
Devonian limestones
d) Ba14
XZ
YZ
0.25mm
C'
C
S
Silurian phyllites
C
S
C'
N=14
Ba8
N= 27
Ba14
N=14
Ba22
K max
K int
K min
Shear C-C' plane
Foliation S plane
Strechting lineation / SC transport direction

ACCEPTED

ACCEPTED MANUSCRIPT

Highlights

- AMS applied to study large shear zones at the brittle-ductile transition

- Changes in AMS ellipsoid related to different strain and deformational conditions

- Shear-reactivation of inherited petrofabrics in shear zones and its correlation with AMS

- Contribution to Cenozoic deformation in Pyrenees (Gavarnie Thrust, Axial zone)

-The constant SSW transport direction obtained from the structural and AMS analysis suggests no vertical rotation for the Gavarnie Unit

ACCEPTED MANUSCRIPT